学位論文

A Study of Magnetohydrodynamic Events Accompanying Magnetic Reconnection in Spherical Tokamak Plasmas

(球状トカマクプラズマにおける
磁気リコネクションを伴う MHD 事象に関する研究)

平成２０年１２月　博士（科学）申請
東京大学大学院新領域創成科学研究科
複雑理工学専攻
東條　寛

Doctoral Thesis

A Study of Magnetohydrodynamic Events Accompanying Magnetic Reconnection in Spherical Tokamak Plasmas

Hiroshi Tojo

Department of Complexity Science and Engineering
Graduate School of Frontier Sciences,
The University of Tokyo

Abstract

Features of MHD (magnetohydrodynamic) instabilities accompanying magnetic reconnection were investigated in the MAST (Mega Ampere Spherical Tokamak) and TST-2 (Tokyo Spherical Tokamak-2) spherical tokamaks (STs). In the presence of finite resistivity, magnetic reconnection occurs and destroys magnetic surfaces. As a result, energy and particles are lost by fast transport along reconnected magnetic field lines. Internal reconnection event (IRE) observed frequently in STs is a typical example of MHD instability involving such a process. This thesis focuses on developing the understanding of IRE with the eventual aim of developing a method to avoid this instability.

In the MAST plasma, there are two types of IREs limiting good performance and triggering plasma collapses. Plasma current spike (increase) due to change of current profile, flattening pressure profile and drop in soft X-ray radiation (SXR), total energy and density. One type accompanies at least two precursors identified as $m = 2/n = 1$ tearing mode and $m = 5/n = 2$ mode. m and n are poloidal and toroidal mode number, respectively. In such IREs, there are inward propagations of decreases on the SXR profile in contrast with a sawtooth crash which propagates from the core to the edge. The powers of such low-n modes show almost maximum values when the collapse starts nearby the $q \sim 2$ rational surface, as determined from the SXR profile. Here q is safety factor. The poloidal structure of the modes obtained from three dimensional filamentary models shows coupling at some poloidal direction and suggests local deformation of the plasma which leads to collapse through magnetic reconnection. Relationship between the magnetic shear and pressure gradient from magnetic reconstruction, suggests some stability effect by the magnetic shear for the avoidance of such IREs. Another type accompanies locked mode ($n = 1$) with the features of ballooning modes at the late stage of IRE.

In the TST-2 plasma, precursors of IRE with $n = 1$ and $n = 2$ localized at the core and generates localized deformation by the modes with constant phase relation during the event and it is very similar to IRE in the MAST plasma. It is found that steep SXR profile is needed for triggering IREs. During the IREs, increase of ion temperature (T_i) of an impurity (OV) starts just after the occurrence of reconnection ($\sim 20\,\mu$s) identified by a spectrometer and enough spatial resolved SXR profile with enough time resolution.

Compared with a three dimensional resistive MHD simulations [T. Hayashi et al., Nuclear Fusion **40**, 721 (2000)], the existence of phase alignment between

the low-n modes, enhancing localized deformation is consistent with the experimental results. Pressure driven ballooning modes with high-n mode also predicted are confirmed. However, the time constant of the growth of the low-n precursor in the experiment is not consistent with the prediction and is much longer by a factor of $\sim 10 - 100$.
A classification of MHD instabilities including IREs in ST plasmas is also given. ELM (Edge localized mode) is one of the MHD instability and shows characteristics of pressure driven mode with high-n mode at the edge of the plasma ($\rho \geq 0.8$). Sawtooth oscillation is instability nearby the $q \sim 1$ rational surfaces, tend to continue again and again in a discharge with $m = 1/n = 1$ mode and leads to collapse near the core without drastic change of the current profile. In contrast with that, IREs show different behaviors in terms of mode structures (strong low-n modes or pressure driven ballooning mode on inside of the plasma) and its time evolution of the profile (collapse from the $q \sim 2$ surface).

A method to determine the poloidal mode number m in a ST based on magnetic probe data is also developed. Perturbed magnetic fields at Mirnov coils are calculated for distributed helical filamentary currents on rational surfaces assuming the maximum current amplitude, m and n and the toroidal location of the filaments. These free parameters are determined from the best fit to the measured signals. The residual error is reduced by a factor of 2 by introducing helical filaments instead of toroidal filaments.

Contents

List of Figures

List of Tables

Chapter 1

Introduction

1.1 Fundamental plasma physics

1.1.1 Plasma

As material is heated to higher temperature, its state changes from solid to liquid to gas. As more energy is added and the temperature is raised further, atoms in the gas are ionized and become the plasma state. The plasma consists of ions and electrons, and is electically neutral on a macroscopic scale. One of the fundamental properties of plasma is shielding of electrostatic potential applied to the plasma. All charged particles interact with each other through the long-range Coulomb force. However, when the electrostatic potential is smaller than the kinetic energy of electrons, the applied electrostatic potential is cancelled by redistribution of many charged particles, and remains effective only within a range of Debye length. The Debye length λ_D can be derived from Poisson's equation and is defined as [1]

$$\lambda_D = \sqrt{\frac{\varepsilon_0 \kappa_B T_e[K]}{e^2 n_e}}\,[\mathrm{m}] = \sqrt{\frac{\varepsilon_0}{e^2}\frac{T_e[\mathrm{eV}]}{n_e}}\,[\mathrm{m}], \tag{1.1}$$

where $\varepsilon_0 = 8.85 \times 10^{-12}\,\mathrm{F/m}$ is the permittivity of free space, $\kappa_B = 1.38 \times 10^{-23}\,\mathrm{J/K}$ is Boltzmann's constant, $e = 1.60 \times 10^{-19}\,\mathrm{C}$ is the electronic charge, T_e is the electron temperature, and n_e is the electron density $[\mathrm{m}^{-3}]$. When the size of plasma is much larger than the Debye length, the plasma is charge neutral. On the contrary, when the size is smaller than the Debye length, individual particles are not shielded electrostatically, and this state is not a plasma but an ensemble of independent charged particles. The number of particles within a cube of Debye length $n\lambda_D^3$ is called the plasma parameter, which indicates the strength of coupling between charged particles. Plasmas

in the regime of $n\lambda_D^3 > 1$ are called weakly coupled plasmas, and plasmas in the regime of $n\lambda_D^3 < 1$ is called strongly coupled plasmas which are usually very dense.

1.1.2 Fusion reaction

It is our goal to handle fusion reactions and derive a large amount of energy on the earth, but fusion reaction rates are extremely low and they occur naturally only under plasma confinement by a huge gravitational potential of stars. In order to supply electric power stably, high efficiency and safety are required. Fusion power reactor has the potential of meeting these requirements. There are many kinds of fusion reactions as listed below [2].

$$ {}_1D^2 + {}_1T^3 \rightarrow {}_2He^4 + {}_0n^1 + 17.6MeV \tag{1.2} $$

$$ D^2 + D^2 \rightarrow He^3 + n^1 + 3.27MeV \tag{1.3} $$

$$ D^2 + D^2 \rightarrow T^3 + H^1 + 4.03MeV \tag{1.4} $$

$$ D^2 + He^3 \rightarrow He^4 + H^1 + 18.3MeV \tag{1.5} $$

Among the reactions listed in Eqs. (1.2)–(1.5), the D-T reaction Eq. (1.2) has the highest reaction cross section with maximum around a deuteron energy of 100 keV (Fig. 1.1). When a nucleus of deuterium (D) fuses with a nucleus of tritium (T), an α-particle is produced and a neutron released. The released α-particle have an energy of 3.6 MeV and heats the plasma, while the 14 MeV neutrons are used to generate power and breed tritium.

The D-T reaction (1.2) requires ions to be accelerated to more than 1000 km/s. Generating a configuration that can confine such high energy ions is essential for sustaining the fusion reaction. In terms of the peak density $\hat{n}$ and the peak temperature $\hat{T}$ of the plasma, the ignition condition can be written as [2]

$$ \hat{n}\hat{T}\tau_E > 5 \times 10^{21}\,\mathrm{m^{-3}\,keV\,s}, \tag{1.6} $$

where τ_E is called the energy confinement time which is defined as the ratio of the total plasma energy to the energy loss rate.

1.1.3 Coulomb collisions

Assume that a sphere with radius a moves with velocity v through a region filled with spheres with radius b with number density n (Fig. 1.2). When the distance between two particles becomes less than $a + b$, a collision occurs. The cross section σ of such a collision is $\sigma = \pi(a + b)^2$. Since the sphere

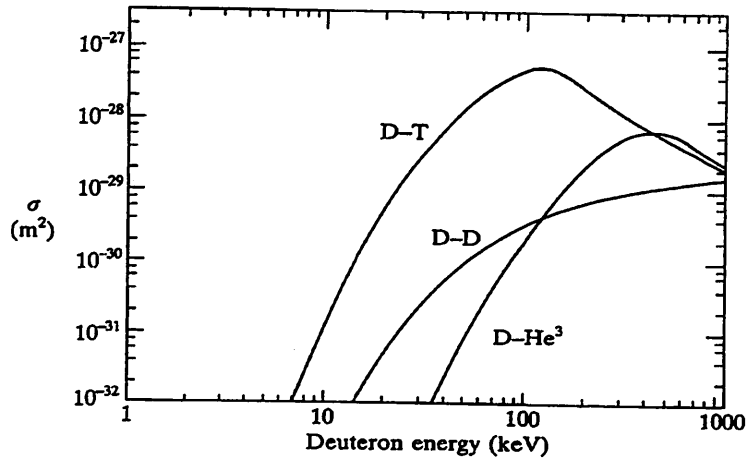

Figure 1.1: Fusion reaction cross-sections. The two D-D reactions have similar cross-sections and the trace plotted is their sum.

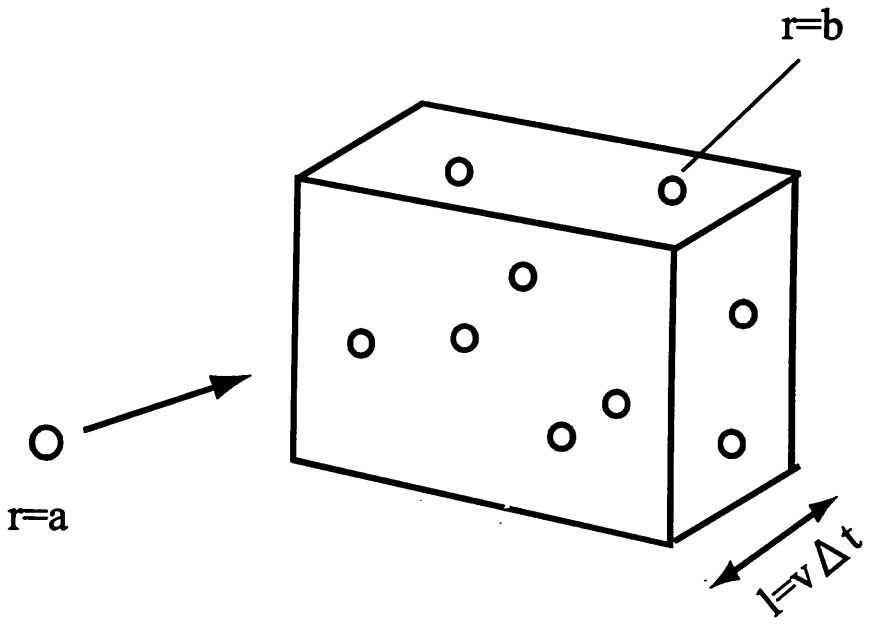

Figure 1.2: Schematic of collision of a test particle with radius a and field particles with radius b.

with radius a moves by distance $l = v\delta t$ during a time interval of δt, the probability of collision with spheres with radius b is

$$nl\sigma = n\sigma v\delta t \tag{1.7}$$

since nl is the possible number of spheres with radius b with which the sphere with radius a can collides with, per unit area of incidence, and $nl\sigma$ is the total cross section for collision per unit area of incidence during the time interval δt. The collision time t_{coll} is expressed as

$$(t_{\rm coll})^{-1} = n\sigma v \tag{1.8}$$

Coulomb collisions are shown schematically in Fig. 1.3. Large angle collisions

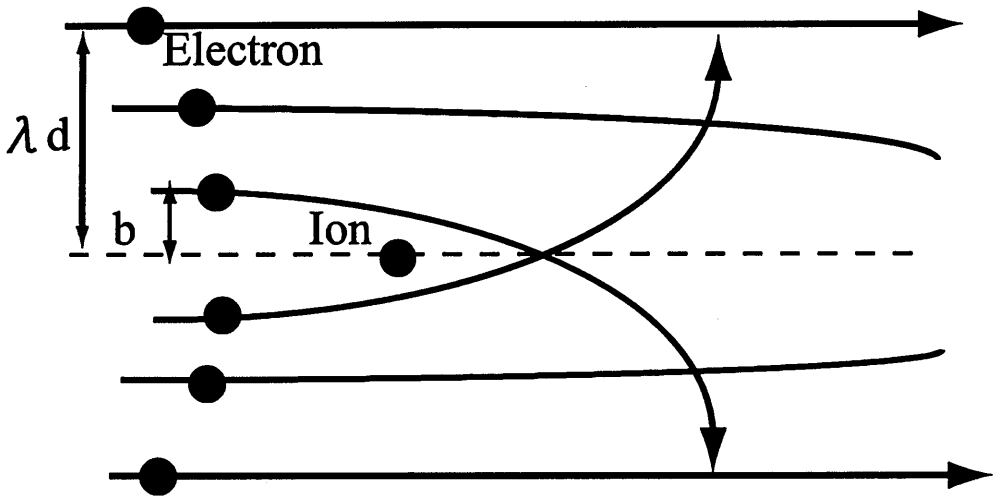

Figure 1.3: Schematic of Coulomb collisions.

occur when the electrostatic potential at the closest approach b is of the order of kinetic energy of the incident electron, i.e.,

$$\frac{Ze^2}{4\pi\epsilon_0 b} = \frac{m_e v_e^2}{2} \tag{1.9}$$

The cross section for large angle Coulomb collisions is $\sigma = \pi b^2$. The collision time is given by

$$(t_{\rm coll})^{-1} = n_i\sigma v_e = n_i v_e \pi b^2 = \frac{n_i\pi(Ze^2)^2 v_e}{(4\pi\epsilon_0 m_e v_e^2/2)^2} \tag{1.10}$$

$$= \frac{Z^2 e^4 n_i}{4\pi\epsilon_0^2 m_e^2 v_e^3}. \tag{1.11}$$

Since the Coulomb force is a long range force, a test particle is deflected by a small angle even by a distant field particle. Coulomb potential of a field particle is not shielded inside the Debye sphere with radius λ_D, and there are many field particles inside the Debye sphere in a usual plasma. Accumulation of many collisions with small angle deflections eventually results in a large deflection. When this effect is taken into account, the Coulomb collision cross section increases by the factor of Coulomb logarithm

$$ln\Lambda \simeq \ln\left(\frac{2\lambda_D}{b}\right) \simeq \int_{b/2}^{\lambda_D} \frac{1}{r} dr \simeq 15 \sim 20. \tag{1.12}$$

The time derivative of the momentum $p_\parallel$ parallel to the direction of incidence is given by use of the collision time $\tau_{ei\parallel}$ as

$$\frac{dp_\parallel}{dt} = -\frac{p_\parallel}{\tau_{ei\parallel}} \tag{1.13}$$

$$\frac{1}{\tau_{ei\parallel}} = \frac{Z^2 e^4 n_i \ln\Lambda}{4\pi\epsilon_0^2 m_e^2 v_e^3} \tag{1.14}$$

where $\tau_{ei\parallel}$ is the deceleration time of the incident electron by ions.

1.1.4 Resistivity

As described later (Sec. 1.1.5),, finite electrical resistivity is essential for magnetic reconnection. The current density j induced by the electric field is [1]

$$j = -en(v_e - v_i) = \frac{e^2 n_e \tau_{ei}}{m_e} E. \tag{1.15}$$

From Ohm's law, $\eta j = E$

$$\eta = \frac{m_e}{e^2 n_e \tau_{ei}} = \frac{m_e^{1/2} Ze^2 \ln\Lambda}{2 \times 45.7\epsilon_0^2} T_e^{-3/2} \tag{1.16}$$

$$= 5.2 \times 10^{-5} Z \ln\Lambda T_e^{-3/2} (\Omega\mathrm{m}), \tag{1.17}$$

where $\ln\Lambda$ is Coulomb logarithm and η is the electrical resistivity of the plasma.

1.1.5 Magnetic reconnection

If the plasma has zero resistivity, the plasma is frozen to the magnetic field-line, and moves with it. However, plasma has a finite resistivity and the

plasma can deviate from the magnetic fieldline. Modes which are stable in an ideal plasma with zero resistivity may become unstable if a finite resistivity is introduced. Ohm's law can be written as

$$\eta \boldsymbol{j} = \boldsymbol{E} + \boldsymbol{V} \times \boldsymbol{B}, \tag{1.18}$$

where $\boldsymbol{E}$ is the electric field. For simplicity, $\boldsymbol{E}$ is assumed to be zero. The current density is $\boldsymbol{j} = \boldsymbol{V} \times \boldsymbol{B}/\eta$, and therefore, the $\boldsymbol{j} \times \boldsymbol{B}$ force is

$$\boldsymbol{F}_s = \boldsymbol{j} \times \boldsymbol{B} = \frac{\boldsymbol{B}(\boldsymbol{V} \cdot \boldsymbol{B}) - \boldsymbol{V}B^2}{\eta}. \tag{1.19}$$

When η tends to zero, this force becomes infinite and prevents the plasma from deviating from the magnetic fieldline. When the magnetic field is small, this force does not become very strong. Even when η is small, the plasma can deviate from the magnetic fieldline. In this situation, magnetic reconnection can occur. Figure. 1.4 illustrates the process of magnetic reconnection. First,

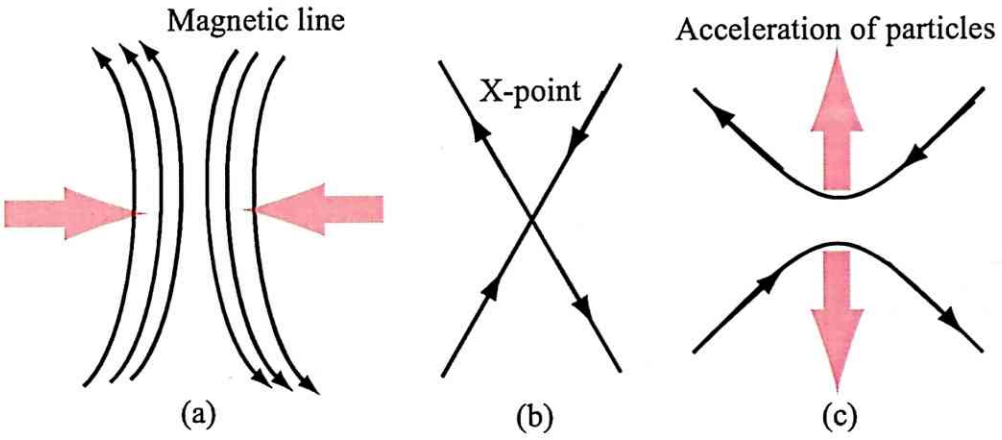

Figure 1.4: Process of magnetic reconnection. The lines indicate magnetic fieldlines. The fieldlines approach each other (a), intersect (b), and finally reconnect (c).

anti-parallel magnetic fieldlines approach each other The fieldlines intersect and makes an "X" shaped configuration. Finally, these field lines reconnect with each other. Subsequently, the straightening of the fieldlines by tension accelerates particles. Part of the magnetic energy is converted to plasma kinetic energy in this process. However, plasma energy and particles could be transported out of the confinement region along the fieldline if the reconnected fieldline escapes the confinement region. It is the purpose of this thesis to study this phenomenon.

1.2 Tokamak and spherical tokamak

1.2.1 Tokamak

Modern fusion studies are mainly performed in toroidal magnetic configurations. An axisymmetric torus is shown in Fig. 1.5. The toroidal direction

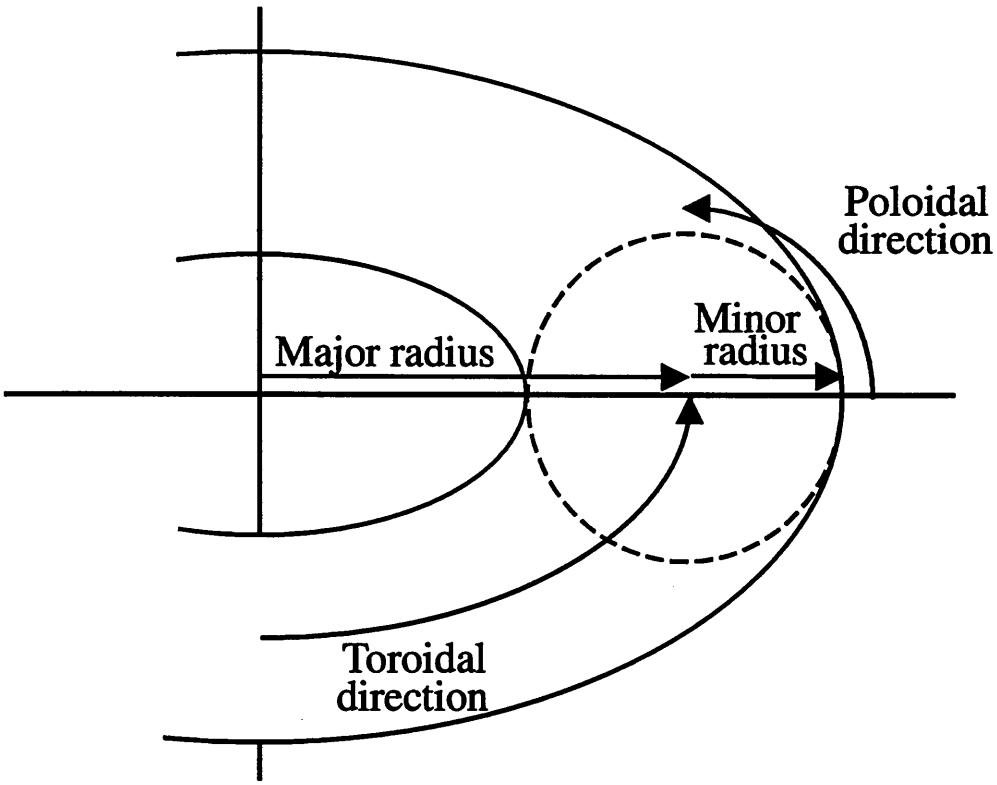

Figure 1.5: Axisymmetric toroidal configuration (tokamak).

is in the major ciucumferential direction whereas the poloidal direction is in the minor ciucumferential direction of the torus. The major radius R_0 is the distance from the symmetry axis to the geometric centre of the poloidal cross-section of the torus, whereas the minor radius a is the horizontal radius of the poloidal cross-section. The aspect ratio A is defined as

$$A = \frac{R_0}{a}. \tag{1.20}$$

A simple toroidal magnetic field has a $1/R$ dependence. The ∇B drift of electrons and ions are in opposite directions vertically [3]. The charge separation induces a vertical electric field E, and both electrons and ions move

towards the outboard side of the torus due to the $E \times B$ drift (Fig. 1.6) [4]. In order to prevent this loss mechanism, it is necessary to connect the

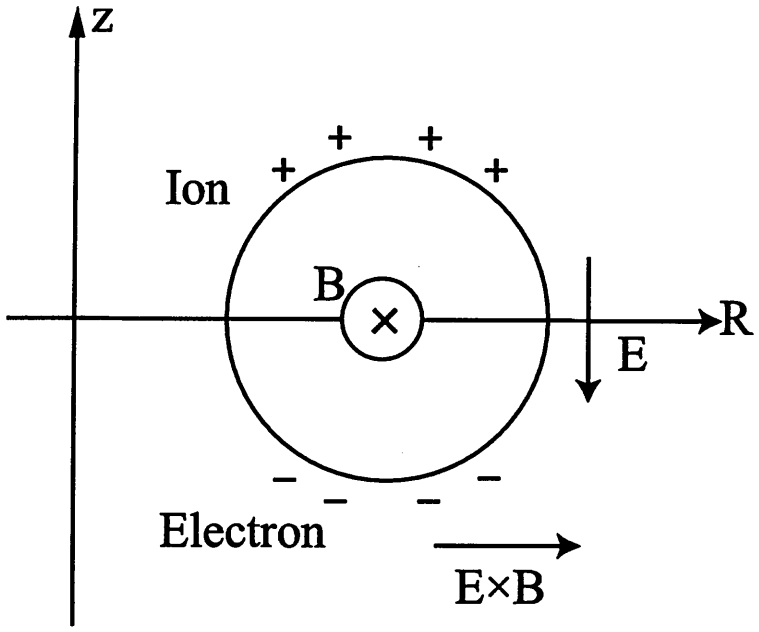

Figure 1.6: $E \times B$ drift in a torus.

magnetic fieldlines from the top to the bottom of the torus. This magnetic field is called the poloidal magnetic field. The poloidal magnetic field in a tokamak is produced by the plasma current in the toroidal direction. High temperature plasmas with good confinement can easily be obtained in the tokamak configuration.

However, the value of beta (β), defined as the ratio of the plasma pressure to the magnetic pressure, is generally low in tokamaks. The highest value of β achieved in a tokamak is $\beta_T \sim 14\%$ in DIII-D [5], where $\beta_T = 2\mu_0 < p > /B_0^2$ and the brackets signify volume average. Low beta implies that to obtain a given fusion power density (which is proportional to p^2), a higher magnetic field and therefore a much more massive reactor is required.

1.2.2 Spherical tokamak

As indicated in Sec. 1.2.1, a critical disadvantage of the conventional tokamak is that β is limited to a low value. Much higher β can be achieved in a low aspect ratio version of the tokamak called the spherical tokamak (ST). ST

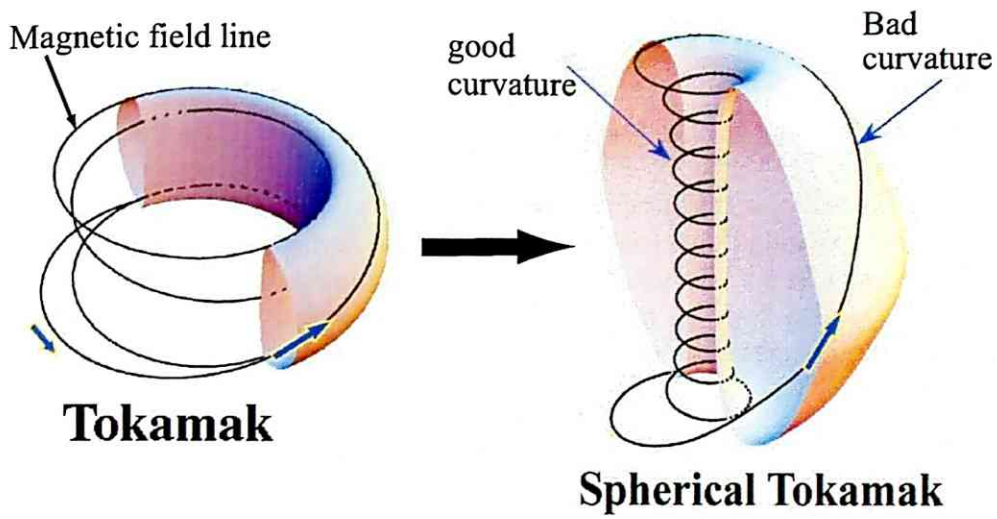

Figure 1.7: Comparison of tokamak and ST.

typically has low aspect ratios, $A < 1.6$ [8][9]. When the aspect ratio is reduced, the plasma moves closer to the symmetry axis, naturally elongates in the vertical direction, and takes a nearly spherical shape. Plasma can be confined by weaker magnetic fields in ST, and therefore ST is attractive for producing fusion energy efficiently. As shown in Fig. 1.7, the pitch angle of the magnetic fieldline is small on the inboard side and large on the outboard side, and particles moving along the magnetic fieldline spends more time on the inboard side where the magnetic field has a good curvature. This is the reason for better stability in ST. High performance in terms of stability and confinement has been investigated in various ST experiments.

1.2.3 Equilibrium in tokamak plasmas

In this section, equilibrium in tokamak plasmas is described and essential parameters for stability analysis are defined. Generally pressure equilibrium is expressed by the following equation of motion.

$$\rho\left(\frac{\partial \mathbf{V}}{\partial t} + (\mathbf{V}\cdot\nabla)\mathbf{V}\right) = -\nabla p + \mathbf{j}\times\mathbf{B}, \tag{1.21}$$

where ρ, $\mathbf{V}$, t, p, $\mathbf{j}$ and $\mathbf{B}$ are density, velocity, time, pressure, current density and magnetic field. In equilibrium, the left hand side of this equation becomes

zero and we obtain

$$\nabla p = \mathbf{j} \times \mathbf{B}. \tag{1.22}$$

This equation shows that $\mathbf{j}$ and $\mathbf{B}$ are both perpendicular to the pressure gradient $\nabla \mathbf{p}$ ($\mathbf{j} \cdot \nabla p = 0$, $\mathbf{B} \cdot \nabla p = 0$). We define the magnetic surface ($\psi(\mathbf{r}) = \text{const.}$) as a surface covered by a magnetic fieldline. By definition a magnetic fieldline does not cross a magnetic surface. The fact that $\mathbf{B}$ is perpendicular to ∇p indicates that p is constant on a magnetic surface. Likewise, j also flows on a magnetic surface according to Eq. 1.22. Since the direction normal to a magnetic surface is perpendicular to the magnetic fieldline,

$$\mathbf{B} \cdot \big(\nabla \psi(\mathbf{r})\big) = 0. \tag{1.23}$$

In equilibrium, p and Ψ are both constant on the magnetic surface, so if we select a magnetic surface, these parameters are uniquely determined. Magnetic surfaces are schematically illustrated in Fig. 1.8. The magnetic axis is

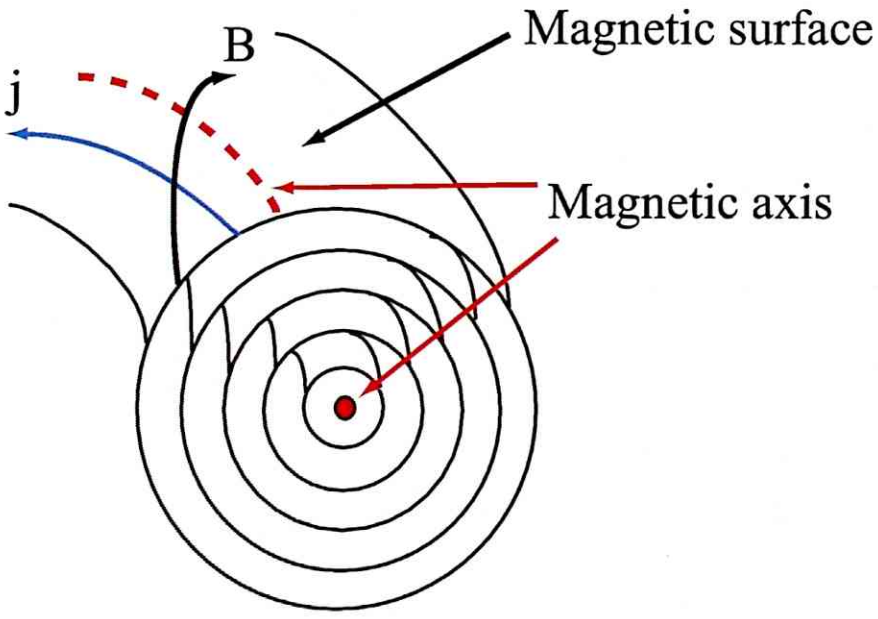

Figure 1.8: Magnetic surfaces and magnetic axis.

defined as the limit of innermost magnetic surface. Magnetic surfaces and the magnetic axis define the equilibrium. Turning now to the tokamak configuration, we can use the condition of toroidal symmetry, $\partial/\partial\phi = 0$. The poloidal flux in cylindrical coordinates can be expressed as $\psi(R, Z) = rA_\phi$,

where A_ϕ is the toroidal component of the vector potential.

$$B_r\frac{\partial(rA_\phi)}{\partial r}+B_\phi\frac{\partial(rA_\phi)}{\partial\theta}+B_z\frac{\partial(rA_\phi)}{\partial z}=0 \tag{1.24}$$

is confirmed by $\mathbf{B}=\mathrm{rot}\mathbf{A}$. This formula is the same as Eq.1.8. Therefore, the poloidal flux is equivalent to the magnetic surface and we can describe p as a function of ψ. From Ampere's law

$$\nabla\times\mathbf{B}=\mu_0\mathbf{j}, \tag{1.25}$$

we obtain

$$-\frac{\partial p}{\partial r}\frac{\partial(rB_\phi)}{\partial z}+\frac{\partial p}{\partial z}\frac{\partial(rB_\phi)}{\partial r}=0. \tag{1.26}$$

Therefore, rB_ϕ is a function of $\mathrm{p}(\psi)$ and we can express

$$rB_\phi=R_0B_0g(\phi), \tag{1.27}$$

where B_0 is the magnetic field at the nominal major radius R_0. $g(\phi)$ is called the toroidal field function, and $g(\phi)=0$ in vacuum (without plasma). Separating the magnetic field into poloidal and toroidal components,

$$B=\frac{1}{2\pi}\nabla\phi\times\nabla\psi+R_0B_0g\nabla\phi. \tag{1.28}$$

From Eq. 1.22, Eq. 1.35 and . 1.29, we obtain the following non-linear partial differential equation

$$r\frac{\partial}{\partial r}\frac{1}{r}\frac{\partial\psi}{\partial r}+\frac{\partial^2\psi}{\partial z^2}=2\pi r\mu_0j_\phi, \tag{1.29}$$

$$\mu_0j=-2\pi\left(r\frac{dp}{d\psi}+\frac{R_0^2B_0^2}{2r}\frac{dg^2}{d\psi}.\right) \tag{1.30}$$

When we eliminate the variable of j_ϕ from these equation, the obtained formula is called the Grad-Shafranov equation [6][7], which is used in various equilibrium reconstruction codes.

1.2.4 Safety factor and current density profile

In an axisymmetric toroidal equilibrium, each magnetic surface has a value of safety factor q associated with it. The magnetic fieldline follows a helical path as it goes round the torus on its associated magnetic surface. By following a field line, if it rotates by toroidal angle $\Delta\phi$ as it makes one poloidal revolution, the safety factor q of this fieldline is defined as

$$q=\frac{\Delta\phi}{2\pi}. \tag{1.31}$$

Thus, if a magnetic fieldline returns to its starting position after exactly one toroidal rotation and poloidal rotation, q−1. At higher q it travels more than one toroidal revolution while it rotates once poloidally. Rational values of q have important roles for stability. If $q = m/n$, where m and n are integers, the poloidal field line returns on itself after m toroidal and n poloidal rotations around the torus. m and n are called poloidal and toroidal mode numbers, respectively.

For calculation of q, equation for the fieldline is needed,

$$\frac{Rd\phi}{ds} = \frac{B_\phi}{B_\mathrm{p}}, \tag{1.32}$$

where ds is the distance moved in the poloidal direction while moving in the toroidal direction by angle ϕ. B_ϕ and B_p are toroidal and poloidal magnetic fields, respectively. Substituting this formula and rewriting Eq. 1.31, we obtain

$$\frac{1}{2\pi} = \oint \frac{1}{R}\frac{B_\phi}{B_\mathrm{p}} ds. \tag{1.33}$$

This integral is over one poloidal turn around the flux surface. Since q is determined by the helical pitch of the magnetic fieldline, we can express q as a function of ψ (flux). Under the assumption of a large aspect ratio, circular croos-section tokamak, the following approximation can be used

$$q = \frac{rB_\phi}{R_0 B_\theta}, \tag{1.34}$$

where r and R_0 are minor and major radii, respectively. The radial profile of q usually shows a minimum at or near the magnetic axis. In the case of a large aspect ratio, circular cross section tokamak, the q profile is determined by the toroidal current density profile $j(r)$ as follows. The poloidal magnetic field is determined by the current through Ampere's law,

$$2\pi r B_\theta = \mu_0 I(r) \tag{1.35}$$

where the current inside the minor radius r is given by

$$I(r) = 2\pi \int_0^r j(\acute{r})\acute{r}d\acute{r}. \tag{1.36}$$

Using the high aspect ratio formula (Eq. 1.34),

$$q(r) = \frac{2\pi r^2 B_\phi}{\mu_0 I(r) R}. \tag{1.37}$$

In particular, at the edge of the plasma ($r = a$),

$$q_a = \frac{2\pi a^2 B_\phi}{\mu_0 I R}. \tag{1.38}$$

Here, I is the total toroidal plasma current. Experimentally, q_a can be calculated from magnetic measurements without difficulty, but the central q value is not easily determined, because the internal current density profile is needed.

The current profile can be expressed by the $q(r)$, or approximately by q_a and the central q value (q_0) which is defined in the limit $r \to 0$ in Eq. 1.37. In this limit $I(r) = \pi r^2 j_0$, where $j_0 = j(0)$, and

$$q_0 = \frac{2B_\phi}{\mu_0 j_0 R}. \tag{1.39}$$

Taking the ratio of q_a to q_0,

$$\frac{q_a}{q_0} = \frac{\pi a^2 j_0}{I} = \frac{j_0}{\langle j \rangle_a} \tag{1.40}$$

where $\langle j \rangle_a$ is the average current density over the whole plasma cross section. This is a standard to represent the current profile when the measured $q(r)$ is not available. If the ratio takes a high value,of the plasma current profile is strongly peaked at the centre of the plasma. Another measure for the peaking factor for current density is the internal inductance defined by

$$l_i = \frac{\overline{B_\theta^2}}{B_{\theta a}^2} = \frac{2\int_0^a B_\theta^2(r) r dr}{a^2 B_{\theta a}^2}. \tag{1.41}$$

Since $B_\theta(r)$ is determined by the current profile, l_i is also useful for expressing the peakedness of current density profile.

1.2.5 Resistive instability

The tearing instability [10] is a resistive instability and appears as magnetic islands in the plasma. As discussed in Sec. 1.1.5, if anti-parallel magnetic fieldlines exist in the plasma, magnetic reconnection can occur under finite resistivity and create magnetic islands. The tearing mode is most easily excited at rational surfaces. When the island width become large, the current density profile flattens in the region of islands and steepens elsewhere, and can lead to a disruption. Magnetic islands are shown schematically in

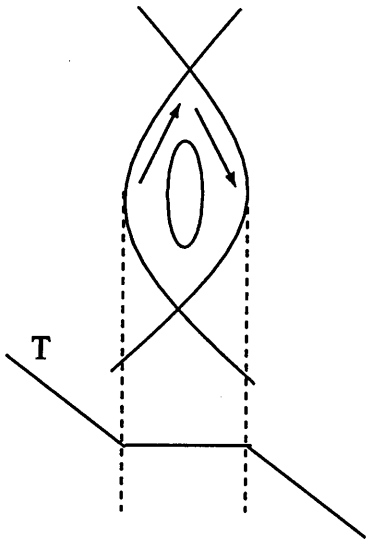

Figure 1.9: Schematic of magnetic islands. Wide magnetic island with a locally flattened temperature profile,

Fig. 1.9. Wide magnetic islands create larger flattened regions on the profile. The flattening is caused by a much faster transport of heat and particles along the magnetic fieldline which became possible by the formation of an island. In high β_p (plasma pressure normalized by the polodial magnetic field pressure) plasmas at low collisionality, the bootstrap current is generated. The bootstrap current is a toroidal current induced by the viscous stress [2] in neoclassical theory, and the driven current density is proportional to the pressure gradient. Wide magnetic islands inhibit the generation of the bootstrap current inside the magnetic island by flattening the pressure profile, This leads to a growth of the neoclassical tearing mode (NTM) and limits the achievable beta. In TFTR, when the volume averaged poloidal beta ($\langle\beta_p\rangle$) exceeded 1, the appearance of $m/n = 3/2$ and $m/n = 5/2$ modes were identified by magnetic fluctuation measurement [11]. The NTM is observed in many tokamaks including DIII-D [12], JT-60U [13], and COMPASS-D [14]. In order to suppress the growth of magnetic island, which is amplified by the loss of the bootstrap current inside the island, current drive by the electron cyclotron wave (ECCD) inside the magnetic island was attempted. The first successful suppression was reported from the ASDEX-U tokamak [15][16][17]. The X-mode EC wave at a frequency of 140 GHz (second harmonic) was excited by injection of $\sim 0.8\,MW$ of RF power. The power was modulated at $15\,kHz$ to drive current only inside the island (O-point phase). The $m/n = 3/2$ NTM intensity was reduced and the increase of β was recov-

ered. Such NTM stabilization experiments were also performed on DIII-D [18] and JT-60U [19][20].

1.2.6 Ideal instabilities

Instabilities which occur in the absence of finite electrical resistivity are called ideal instabilities. Several types of ideal instabilities are described in this subsection.

Interchange instability

The boundary between the vacuum region ($x < 0$) and the plasma region ($x > 0$) is assumed to be at $x = 0$, and the direction of the magnetic field **B** is taken to be along the z axis. (See Fig. 1.10) When there is acceleration

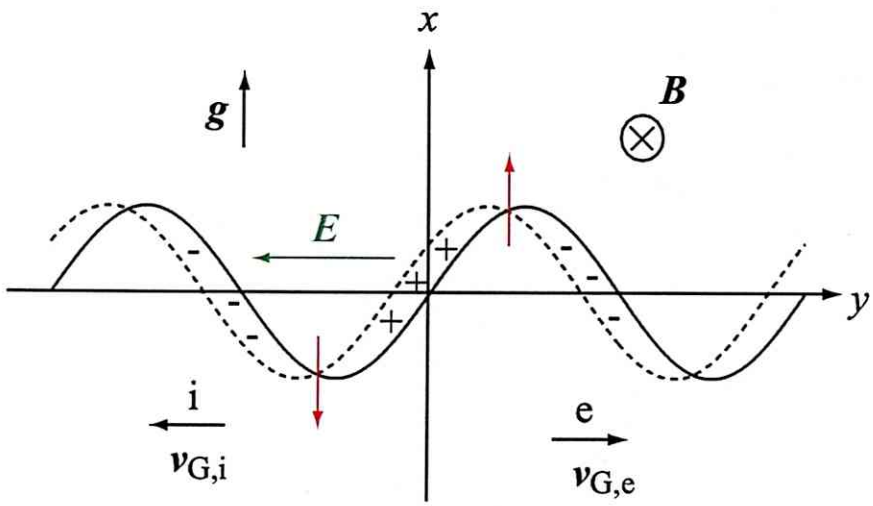

Figure 1.10: Ion and electron drifts and the resultant electrric field for interchange instability [1].

g induced by the density and/or pressure gradient, ions and electrons in the plasma drift toward opposite directions [1].

$$\mathbf{v}_{G,i} = \frac{M}{e}\frac{\mathbf{g} \times \mathbf{B}}{B^2} \tag{1.42}$$

$$\mathbf{v}_{G,e} = -\frac{m}{e}\frac{\mathbf{g} \times \mathbf{B}}{B^2} \tag{1.43}$$

If we assume that the plasma boundary is deformed by the following perturbation,

$$\delta x = a(t)\sin(k_y y) \quad . \tag{1.44}$$

charge separated electrons and ions drift and induce electric fields ($\mathbf{E}$) shown in green. The resultant $\mathbf{E} \times \mathbf{B}$ drift enhances the original perturbation if the acceleration $\mathbf{g}$ is directed towards $x > 0$. This type of instability is called the interchange instability or the flute instability.

Ballooning instability

Another type of interchange instability arises in a toroidal magnetic configuration. We consider the acceleration g as the force exerted by the pressure gradient (∇P_0). The centrifugal force due to the curvature of the magnetic fieldline acts in the direction to enhance the perturbation on the low field side of the torus. If we assume that the plasma initially in a region of flux tube 1 with pressure P_1 and volume V_1 moves to another region of flux tube 2 with P_2 and V_2 as illustrated in Fig. 1.11, the change of internal energy for flux tube 1 can be written as

$$[P_1(V_1/V_2)^\gamma V_2 - P_1 V_1]/(\gamma - 1), \tag{1.45}$$

where the adiabatic gas law, $P_2 = P_1(V_1/V_2)^\gamma$ was used. Assuming $P_2 =$

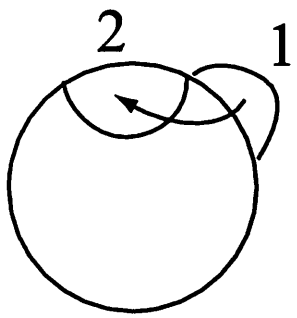

Figure 1.11: Image of plasma cross-section with magnetic tubes 1 and 2.

$P_1 + \delta P$ and $V_2 = V_1 + \delta V$, the change in the total energy is

$$\delta W = \gamma P_1(\delta V)^2/V_1 + \delta P \delta V. \tag{1.46}$$

A sufficient condition for stability is

$$\delta P \delta V > 0. \tag{1.47}$$

The volume of the flux tubes can be expressed as $\int S(l)dl$, where S and dl are the cross sectional area and the differential line segment along the flux tube, respectively. Since $B(l)S(l) = \Phi$ and

$$V = \Phi \int \frac{dl}{B(l)}, \tag{1.48}$$

we can rewrite the stability condition Eq. 1.47 as

$$\delta \int \frac{dl}{B(l)} < 0. \tag{1.49}$$

This formula is called the minimum B stability condition, and indicates that the magnetic field averaged along the flux tube increases as we move away from the centre of the plasma. As shown in Fig. 1.7, flux tubes in tokamak plasmas experience good and bad curvature regions. Perturbations tend to grow in the bad curvature region and balloon out. Such pressure driven mode localized in the bad curvature region is called the ballooning mode. The ballooning mode was observed in TFTR as described in Sec. 2.2.

Kink instability

The kink instability leads to a kinking of the magnetic surface and the plasma boundary. The driving force is the radial gradient of the toroidal field at low β. If we assume a kinking perturbation in a cylindrical plasma as shown in Fig. 1.12, the azimuthal magnetic field (B_θ) becomes stronger in the concave region. The longitudinal field (B_z) has a stabilizing effect due to tension

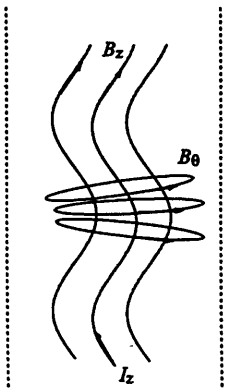

Figure 1.12: Schematic of kink instability.

of the magnetic field. When the drive from B_θ outweighs the stability effect from B_z, the perturbation grows and the plasma is deformed. This instability is called the kink instability.

1.2.7 Sawtooth oscillation in tokamaks

The sawtooth oscillation [21][22] is one of the most notable instabilities in tokamak experiments. In the first observation shown in Ref. [22], the soft X-ray radiation (SXR) profile showed periodic collapses in the core of the plasma. The same behaviour can be observed in the ion temperature, electron temperature and density profiles. The mode structure of the precursor oscillation has been identified as the $m/n = 1/1$ internal kink mode. Models to describe the mode behaviour are classified into three types.
1. Full reconnection model [23][24]:
A complete exhaust of plasma pressure and current density occurs through reconnection along the entire toroidal circumference. Reconnection is initiated by a pressure driven instability. After reconnection, the hot region shrinks over the time scale of collapse.
2. Quasi-interchange model [25]:
The cooler plasma flows into the plasma core and the hot region evolves into a crescent shape due to a strong distortion of the magnetic surface by the $m/n = 1/1$ mode that results from the low magnetic shear in the core of the plasma. SXR tomography suggests that the shape of the hot region is a crescent in JET experiment [26][27]. However since the number of detectors was limited, there is an uncertainty for the shape in the core.
3. Ballooning mode model [32]:
In high β plasmas, a toroidally localized high-n ballooning mode can be driven unstable by the local steep pressure gradient induced by low-n modes. Through non-linear coupling, high-n modes produce a toroidally localized pressure bulge and destroy the magnetic surface.

In order to confirm the mode behaviour, a two dimensional T_e imaging system based on electron cyclotron emission (ECE) was employed in the TEXTOR tokamak [28][29][30]. Details of the measurement is explained in [31]. An example of the $\tilde{T}_e$ profile is shown in Fig. 1.13 from [28]. The shape of the hot region is very similar to that predicted by the full reconnection model. In the model the hot region in the core and the cold region from outside the inversion radius are exchanged gradually until the loss of the the hot spot through non-localized reconnection. However, until the time of the fifth frame, the hot region is rotating but never crosses the black curve in the figure, which is inconsistent with the prediction. The black curve is the inversion radius where the temperature fluctuation shows different polarity during the collapse. The hot plasma crosses the black curve from the sixth frame in a short time scale, which is similar to the prediction of the ballooning mode model. Therefore, more than one model is needed to

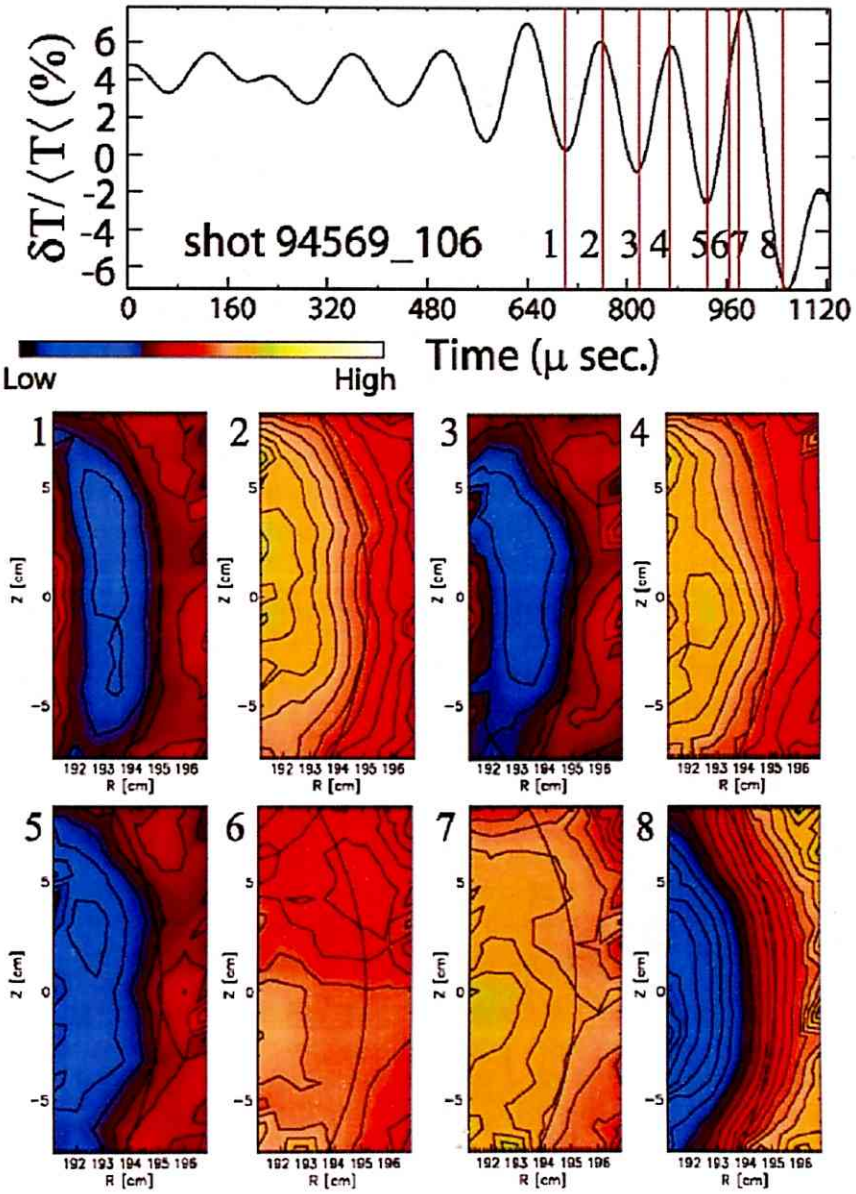

Figure 1.13: Two dimensional $\tilde{T}_e$ profile during sawtooth oscillation in TEXTOR [28].

explain the evolution.

1.2.8 Plasma heating

Heating of the plasma is essential for realizing high fusion reaction rates because the reaction rate depends strongly on the ion temperature. In this section two heating methods are described.

Ohmic heating

Almost all tokamaks employ ohmic heating for initial heating. This method uses a coil (usually a solenoid) lodated on the inboard side of the torus to generate an inductive electric field in the toroidal direction (loop voltage) to drive the plasma current. At low electron temperature, Ohmic heating is very effective for heating the plasma. In large tokamak experiments, plasmas with electron temperatures of over 1 keV can be created easily. However this method becomes ineffective at higher temperatures, because the resistivity decreases as $T_e^{-3/2}$. The ohmic heating power density P_o can be expressed as

$$P_o = \eta j^2 \tag{1.50}$$

where η is the resistivity of the plasma and j is current density. In some cases the magnitude of j is limited by MHD instability. One standard MHD stability condition in tokamaks is given by $q_a > 2$. Using the expression for q_a in high aspect ratio approximation Eq. 1.34 and Ampere's law Eq. 1.35, the average current density must satisfy

$$\langle j \rangle < \frac{1}{\mu_0}\frac{B_\phi}{R}. \tag{1.51}$$

Neutral beam injection

Neutral beam injection is one of the most effective ways to heat the plasma. Once the injected neutral beam particles are ionized in the plasma, the resulting fast ions slow down by Coulomb collisions. As the slowing down occurs, energy of the fast ions is transferred to plasma particles, thus heating electrons and ions. The heating power P is [2].

$$P = m_b A_D \left(\frac{2m_e^{1/2} E_b}{3(2\pi)^{1/2} T_e^{3/2}} + \frac{m_b^{2/3}}{2^{3/2} m_i E_b} \right). \tag{1.52}$$

where

$$A_D = \frac{ne^4 \ln \Lambda}{2\pi\epsilon_0^2 m_b^2}, \tag{1.53}$$

and m_b, E_b, m_e, m_i and T_e are mass of the injected atom, injected beam energy, electron mass, ion mass and electron temperature, respectively. At high beam ion energy, electron heating is dominant, but as the beam ions slow down, ion heating becomes dominant. Electron mass is much smaller than the ion mass, and collisions with electrons cause only a small scattering of the beam ions. On the contrary, collisions with the ions is accompanied by scattering of the beam ion velocities principally perpendicular to the initial direction. This spreading of the perpendicular velocities itself contributes a "heating" by the beam ions which will ultimately contribute to the plasma energy.

1.2.9 High confinement mode (H-mode)

Two of the most common confinement modes are the high confinement mode (H-mode) and the low confinement mode (L-mode). H-mode typically has a factor of two longer energy confinement time (τ_E) compared to L-mode. In L-mode, the confinement time degrades with increased heating power, and is expressed by scaling laws such as the.ITER89-P ($\tau_E^{ITER89-P}$) scaling [33],

$$\tau_E^{\mathrm{ITER89-P}} = 0.048 \frac{I_p^{0.85} R^{1.2} a^{0.3} \kappa^{0.5} (n/10^{20})^{0.1} B_T^{0.2} A^{0.5}}{P^{0.5}} \mathrm{s}. \tag{1.54}$$

Here, I_p, κ, n, B, A and P are the plasma current [MA], elongation, density, toroidal magnetic field, aspect ratio and input power [MW], respectively. H-mode was discovered in the ASDEX tokamak in Germany[34]. It was found that a pedestal develops in the density profile in the edge region as shown in Fig. 1.14 [35], and the confinement improves by a factor of two when sufficient heating power was applied. In ELMy H-mode, the edge localized mode (ELM) periodically exhausts energy and particles in short bursts, detected as rapidly growing magnetic fluctuations and H_α bursts. The confinement time in ELMy H-mode plasmas is expressed by[36]

$$\tau_E^{\mathrm{ELMy}} = 0.0365 \frac{I_p^{0.97} B_T^{0.08} (n/10^{20})^{0.41} M^{0.20} R^{1.93} \varepsilon^{0.23} \kappa^{0.67}}{P^{0.63}} \mathrm{s} \tag{1.55}$$

where ε is inverse aspect ratio. In ELM-free H-mode plasmas,

$$\tau_E^{\mathrm{ELM-free}} = 0.0314 \frac{I_p^{0.94} B_T^{0.27} (n/10^{20})^{0.34} M^{0.43} R^{1.98} \varepsilon^{0.1} \kappa^{0.68}}{P^{0.68}} \mathrm{s}. \tag{1.56}$$

Edge Localized Modes

In many experiments, spikes of H_α (or D_α) emission are observed during the H-mode phase. These are caused by particle loss due to an instability localized in the edge of the plasma called the edge localized mode (ELM). More

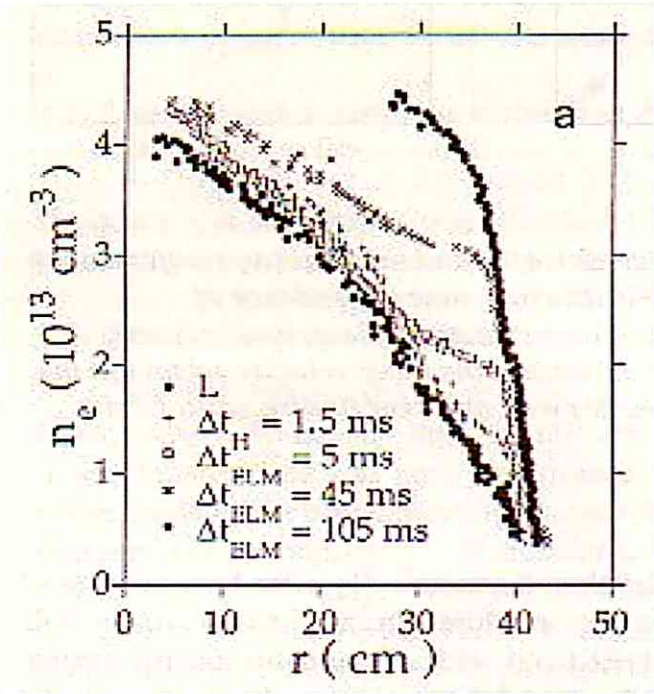

Figure 1.14: Development of the edge density profile measured by reflectometry, from L-mode, 0.5 ms after the transition, to a quiescent phase which developed after an ELMy phase [35].

than three types of the ELMs have been found. The first classification of ELMs was given by the DIII-D group [5].
1. Type-I ELM
The ELM repetition frequency increases with heating power. The level of broadband magnetic and density turbulent fluctuations increases prior to a type I ELM. Ideal ballooning analysis shows that the plasma edge is always close to the stability limit. Type I ELMs appear as isolated sharp bursts on the D_α-signal.
2. Type-II ELM
In a DIII-D discharge exhibiting type I ELMs, the ELM character changes when the shape of the plasma cross section is changed towards higher elongation and triangularity. The ELM repetition frequency becomes more frequent and the magnitude of the D_α-burst decreases. In this case, the plasma edge is found to be in the connection regime between the first and the second stable region of the ballooning diagram.
3. Type-III ELM
The ELM repetition frequency decreases with heating power. A coherent magnetic precursor oscillation with 50–70 kHz is observed on magnetic probes located close to the plasma in the outboard midplane. Toroidal mode numbers of $n = 5$–10 were inferred.
Pressure driven modes destabilized by the increased pressure gradient near the edge is believed to be the cause of ELM. The notable point is that this instability occur near the edge of the plasma.

1.3 X-ray radiation from plasma

1.3.1 X-ray

X-ray is an electromagnetic (EM) wave with wavelength in the range 10^{-12} to 10^{-8} m. X-ray is emitted when energetic electrons or other charged particles collide with some substance, or when irradiated by X-ray or γ-ray with higher energy. EM waves with high energy have characteristics of a particle (photon), while lower energy EM waves have characteristics of a wave (diffraction and interference). In the range of soft X-ray ($\sim 10^{-8}$ m), photons are absorbed by air and must be measured in vacuum.

1.3.2 X-ray generation mechanisms

There are three mechanisms of X-ray generation as illustrated in Fig. 1.15. Bremsstrahlung is emitted when an electron is decelerated by an ion. Ac-

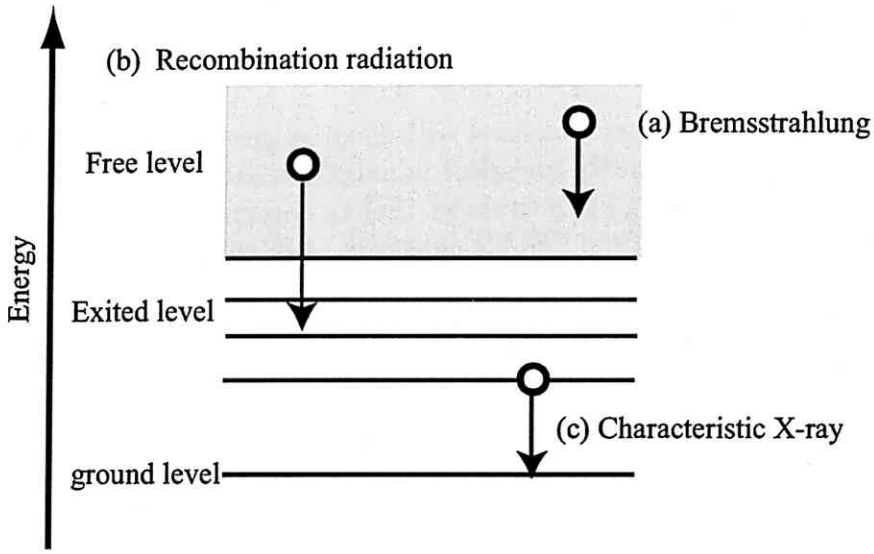

Figure 1.15: X-ray generation mechanisms: (a) Bremsstrahlung, (b) recombination radiation, (c) characteristic X-ray.

celerated charges give off electromagnetic radiation, and when the energy of the bombarding electrons is high enough, the radiation is in the X-ray region. It is characterized by a continuous spectrum because both initial and final states are free energy levels (continuum). Recombination radiation is emitted when a free electron is captured by an ion. It is also characterized by a continuous spectrum. Characteristic X-rays are emitted from heavy elements when an electron in an excited bound state makes a transition to a lower energy bound state. Characteristic X-ray emission typically involves bombardment of metallic impurity ions by high energy electrons. The bombarding electrons can eject an electron from an inner shell, and the vacancy is filled quickly by an electron from an excited state. The emitted X-ray has a sharply defined frequency (wavelength) associated with the energy difference between the two energy levels.

1.3.3 Radiation from plasma

Under the assumption that the electron velocity distribution is Maxwellian, the energy spectrum of bremsstrahlung emission (photon number per unit volume and time) is given by [37]

$$\frac{dP_B}{dE} = 3 \times 10^{-3} n_e^2 \frac{Z_{\text{eff}}}{\sqrt{T_e}} g_{\text{ff}}(T_e, E) exp\left(-\frac{E}{T_e}\right) [\text{m}^{-3}\text{s}^{-1}] \qquad (1.57)$$

where $n_e\,[m^{-3}]$, $E\,[keV]$, $T_e\,[keV]$ and $g_{ff} \sim 1$ are electron density, photon energy, electron temperature, and the Gaunt factor for free-free transition, respectively, and Z_{eff} is the effective ion charge number defined as

$$Z_{\rm eff} = \frac{\sum_i Z_{\rm i}^2 n_{\rm i}}{n_{\rm e}}. \tag{1.58}$$

The energy spectrum of recombination radiation is given by

$$\frac{dP_R}{dE} = 3 \times 10^{-3} \frac{n_{\rm e} n_{\rm i}^{(z_i)}}{\sqrt{T_{\rm e}}} z_{\rm i}^2 g_{\rm fb}(T_e, E) \exp\left(\frac{E}{T_{\rm e}}\right) \frac{\xi}{n^3} \frac{\chi_{\rm i}}{T_{\rm e}} exp\left(\frac{\chi_i}{T_{\rm e}}\right) [{\rm m}^{-3}{\rm s}^{-1}] \tag{1.59}$$

However, this expression ignores processes involving highly-excited levels. It indicates the intensity of recombination radiation from z_i to $(z_i - 1)$ ion. $g_{fb} \sim 1$ is the Gaunt factor for free-bound transition. χ_i, n, and ξ are ionization energy of the $(z_i - 1)$ ion, the main quantum number in cases of recombination to the ground level, and the statistical weight of the ground level for recombination to nl level, given by

$$\xi = 2(2l+1) - (\mu - 1) + 2 \sum_{l'=l+1}^{n-1} (2l'+1) \tag{1.60}$$

where the first term and the second term are statistical weights in nl-level with μ electrons and for the case of $l' > l$, respectively.

The intensity of radiation from a high-temperature plasma is expressed by the sum of bremsstrahlung and recombination radiation. It is known theoretically that the radiation spectrum includes a factor $\exp(-E/T_e)$. T_e can be determined from the slope of a semi-log plot of X-ray intensity as a function of photon energy.

Chapter 2

Review of previous studies and thesis objectives

2.1 Internal reconnection events

2.1.1 START experiments

START (Small Tight Aspect Ratio Tokamak) [38][39][40] at Culham, U.K. is the first ST with auxiliary heating that demonstrated high performance (high β, H-mode, etc.) and unique advantages of ST over the conventional tokamak. Relaxation phenomena were often observed, and these were named Internal Reconnection Events (IREs). IREs accompany a positive spike in the plasma current ($\Delta I_p/I_p \sim 10\%$–15%) along with a negative loop voltage spike, and bursts of H_α and CIII radiation. Rapid drops in SXR and line integrated electron density as well as a loss of stored energy (by typically 30%–40%) were often observed after a current spike, but signatures of current terminating disruption were not observed, and the current returned to its pre-IRE level. It is believed that IREs in STRAT limited the operation space at high density and low-q. Time evolutions of the plasma current and density in a discharge with an IRE which limited the achievable density (at $t = 0.035\,s$) is shown in Fig. 2.1 from Ref. [41]. The plasma elongation increases at an IRE, and therefore q_{95} increases and stabilize low-m instabilities. Typical START discharges with NBI heating evolve in this way, usually experiencing multiple IREs as the current decays. A reduction of the toroidal magnetic field during the discharge is found to lead to a large increase in β, but these discharges accompany MHD instabilities and profile changes. The toroidal field can be reduced until the low-q limit is reached. Results of kink mode stability studies using the ERATO code[46] are summarized in Fig. 2.2. These are for a pressure-less ($\beta = 0$) model, and for a natural divertor config-

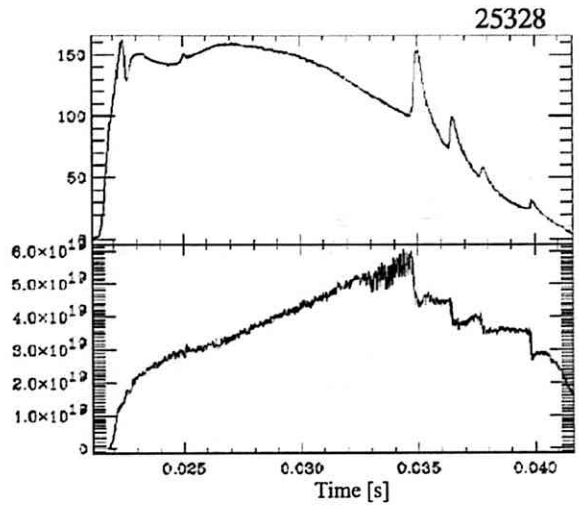

Figure 2.1: IRE which occurred at the highest normalized density, $n_G = \pi a^2 n_e / I_p \sim 0.91$.

uration with the plasma limited on the centre column. These results suggest that as the aspect ratio A is reduced, the requirement $q_s = 2$ applicable to conventional tokamaks becomes more restrictive, and that $q_s = 4$ may be required for $A = 1.2$, although this is more than compensated by the increase in the achievable I/aB at low A. Increasing the pressure does not change this picture significantly.

In order to understand the evolution of plasma deformation during an IRE, images of visible light emission from the plasma were recorded by a CCD (charge coupled device) camera. Examples are shown in Fig. 2.3 [53]. Brighter regions correspond to relatively cool parts of the plasma. Figure 2.3(a) is taken by a monochromatic CCD camera, which has a good time resolution (about 30 μs), at an early stage of IRE. A bright helical structure is observed to extend in the periphery from the top to the bottom of the torus. A filamentary structure is observed as bright stripes in the middle of the image (denoted by B). An overall distortion is captured in Figs. 2.3(c) and (d), which appear in slightly later stages of IRE. Note that these two images were taken on different discharges, It can be seen in Fig. 2.3(c) that the shapes of the poloidal cross section on both sides are largely tilted. In Fig. 2.3(d), the shapes of the poloidal cross section are fat (horizontally elongated) on the right side, and thin (vertically elongated) on the left side.

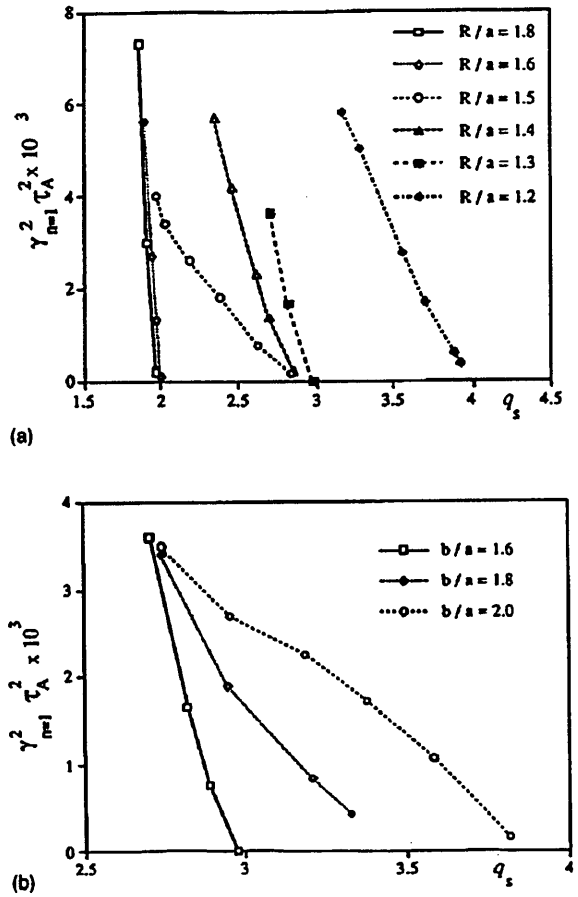

Figure 2.2: $n = 1$ external kink growth rate ($\beta = 0$ model) from Ref. [40] for triangularity $\delta = 0.25$, current profile $\langle J_\phi \rangle \sim (1 - \psi)$, $q(0) = 1.15$, with remote wall For (a) $R/a = 1.2 - 1.8$ and (b) elongation $\kappa = 1.6 - 2.0$ at $R/a = 1.3$.

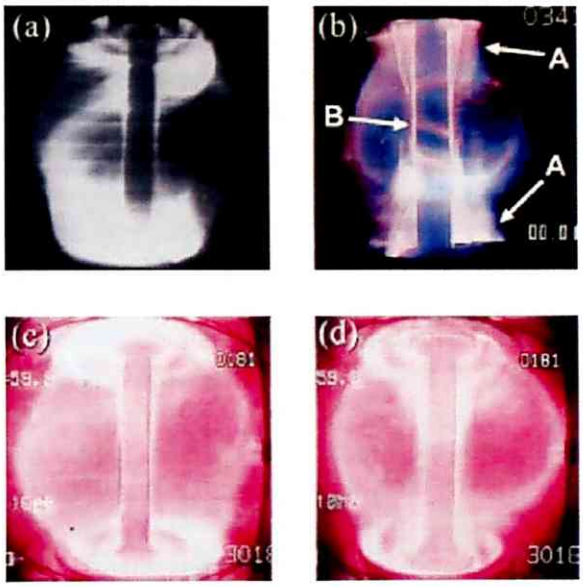

Figure 2.3: CCD camera images of START plasma when IRE is observed. (a) Appearance of localized deformation, (b) appearance of conical layers at the top and the bottom of the torus (denoted by A) and filaments (denoted by B), (c) appearance of a tilted distortion, (d) appearance of an asymmetric distortion.

2.1.2 NSTX experiments

Features of IRE in NSTX (National Spherical Torus Experiment) [42] at Princeton, USA have been investigated by I. Semenov et al. [43]. The main device parameters of NSTX are shown in Table 2.1. In order to investigate

parameter	value
Major radius R	$\sim$ 0.85 m
Minor radius a	$\sim$ 0.65 m
Aspect ratio A	$\sim$ 1.5
Elongation κ	1.7-3.0
Triangularity δ	0.3-0.8
Toroidal magnetic field B_t	$\sim$ 0.55 T
Plasma current I_p	$\sim$ 1.5 MA

Table 2.1: Typical NSTX parameters

the profile and mode evolutions, magnetic probe signals and SXR data were used. Experimental set-up is shown in Fig. 2.4. Two sets of 16-channel hor-

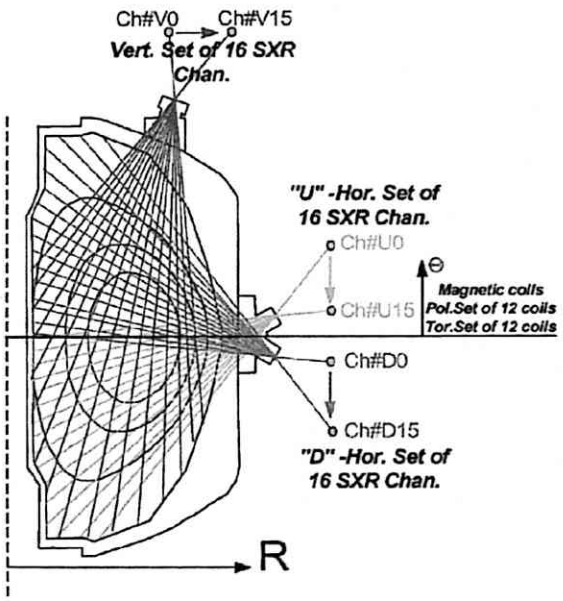

Figure 2.4: Diagnostic geometry in NSTX

izontal array and a 16-channel vertical array were used to measure the SXR

emission profile, and 24 magnetic coils were used to measure dB_θ/dt and determine the toroidal number n and poloidal mode structure. The vertical SXR array had a 0.3 μmTi foil as a filter, and measured photons in the energy range 0.1 – 10 keV. Two horizontal arrays had 10 and 100 μm Be foils and measured photons with energy above 1 and 2 keV, respectively. They classified reconnection events into minor and major IRE. Major IREs occur near the end of the discharge, whereas minor IREs occur earlier.

A typical discharge with a minor IRE is shown in Fig. 2.5. An I_p spike was observed from 218 ms. Before this time, a fluctuation on SXR profile with a frequency of about 2 kHz shows $m = 1/n = 1$. The spatial extent of perturbation expands, and the positive SXR perturbation moves to the outside of the torus. Right before the current spike, magnetic and SXR oscillations stop for about 2 ms (mode locking), and then an internal crash is observed by the SXR vertical camera measuring lower energy photons (Fig. 2.5(f)). After the IRE, increases of peripheral impurity radiation caused by energetic electrons escaping from the plasma, were observed. They focused on the behaviour of plasma current (I_p) during the growth of the SXR perturbation. It increases slightly. This can be a result of reduced internal inductance l_i, i.e., current profile flattening. During and after the crash of SXR emission, an increase of I_p by $\sim 4\%$ is observed, indicating a decrease in l_i and a partial expulsion of the poloidal magnetic flux from the plasma.

An example of a major IRE ending in a disruption is shown in Fig. 2.6. This IRE is preceded by a spontaneous locked mode (Phase I). The collapse which occurs 5 ms later with the loss of heat and particles is clearly visible in the SXR profile (Phase II). During Phase III, the amplitude of MHD activity increases (dB/dt from Fig. 2.6(b)), and in Phase IV the penetration of impurities from the wall to the plasma increases (Fig. 2.6(e)). In this IRE, I_p shows an increase, but then decreases because the central cooling changes the resistivity significantly. To understand the ST-specific characteristics of this instability, it is very important to compare parameters of STs and conventional tokamaks. They compared the fast thermal quench duration measured by SXR to those in conventional tokamaks documented in the ITER physics basis [44]. The result shows factors of 5–10 difference for major IREs (Fig. 2.7). However, they could not understand what plasma parameters lead to such long thermal quench times in NSTX. They found that τ_{tq} is long at $q_{95} \sim 5$ and supposed that this is the source of such long thermal quench times. They inferred dependences on the coupling between internal and external modes. For example, they thought that the $m/n = 4/2$ mode at $q = 2$ (internal mode) and the $m/n = 4/1$ mode at $q = 4$ (external mode) could couple easily. On the contrary, it is not easy for the $m/n = 5/1$ mode at $q_{95} = 5$ to couple with serious internal modes such as the $m/n = 2/1$

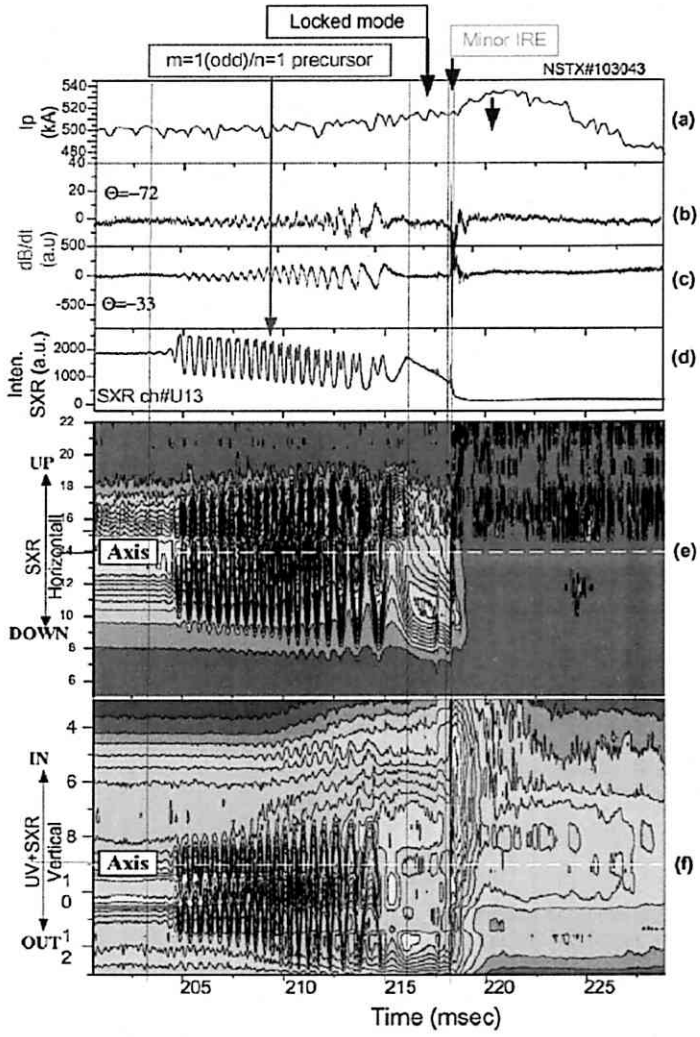

Figure 2.5: Discharge with a minor IRE (No.103043) [43]. (a) Plasma current I_p, (b) dB_θ/dt at θ=-72°, (c) dB_θ/dt at $\theta = -33°$, (d) SXR signal from the plasma (Ch. 13, close to the plasma centre), (e) and (f) SXR emission profiles measured by horizontal and vertical arrays.

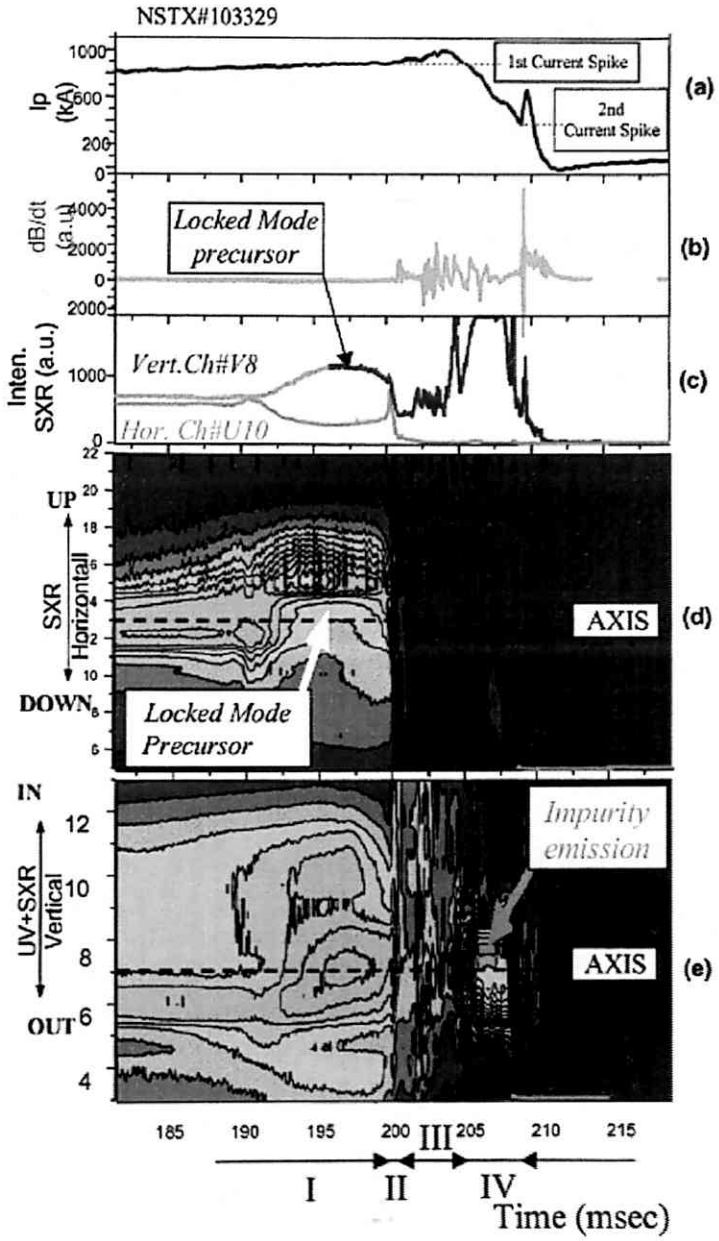

Figure 2.6: Discharge with a minor IRE (No.103329) [?]. (a) Plasma current I_p, (b) dB_θ/dt, (c) vetical and horizontal SXR signals (d), (e) SXR emission profiles measured by horizontal and vertical cameras.

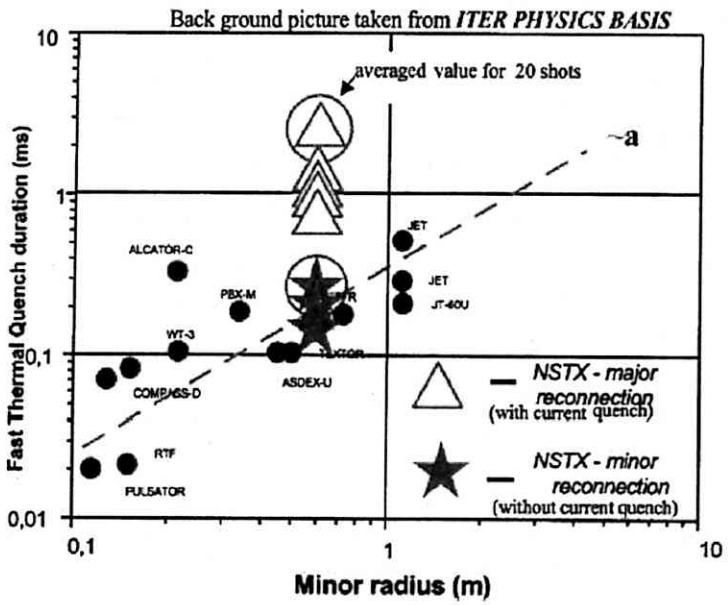

Figure 2.7: The fast thermal quench times τ_{tq} for NSTX compared to those observed in several tokamaks [45]

and $m/n = 3/1$ modes.

2.1.3 HIT-II experiments

The Helicity Injected Tokamak-II (HIT-II) device is a low aspect ratio tokamak designed to study CHI (coaxial helicity injection) [47][48] as well as transformer current drive. The main device parameters of HIT-II are shown in Table 2.2 [49]. In the HIT-II, they focused on the ion temperature increase

parameter	value
Major radius R	~ 0.3 m
Minor radius a	~ 0.2 m
Aspect ratio A	~ 1.5
Toroidal magnetic field B_t	~ 0.5 T
Plasma current I_p	< 225 kA

Table 2.2: Typical HIT-II parameters.

during IRE measured by ion Doppler spectroscopy [50]. The principle of the

Doppler spectroscopy will be described in Chap. Doppler. A 16-channel photomultiplier array was used to measure the ion temperature and the flow velocity. The measurements used the OV line at 278.1 Å. because it is the brightest line in most HIT-II discharges. The sight line for the measurement can be selected on the device mid-plane at any of the 20 tangentially viewing ports (10 on each side of the central column). In addition, a radially viewing mid-plane port is also available. CHI-initiated transformer-driven (Ohmic) discharges show elevated ion temperatures of $T_i = 150$–$200\,eV$ during the CHI phase. However, during the Ohmic phase $T_i = 50 - 100\,eV$. IREs occur in both the transformer driven phase and the current decay phase. IREs during the transformer driven phase are accompanied by a rapid rise in T_i of $50 - 75\,\text{eV}$. Figure 2.8 presents OV temperature for one such discharge. During the CHI pulse, $T_i = 160\,\text{eV}$ before cooling to 50 eV as CHI is turned

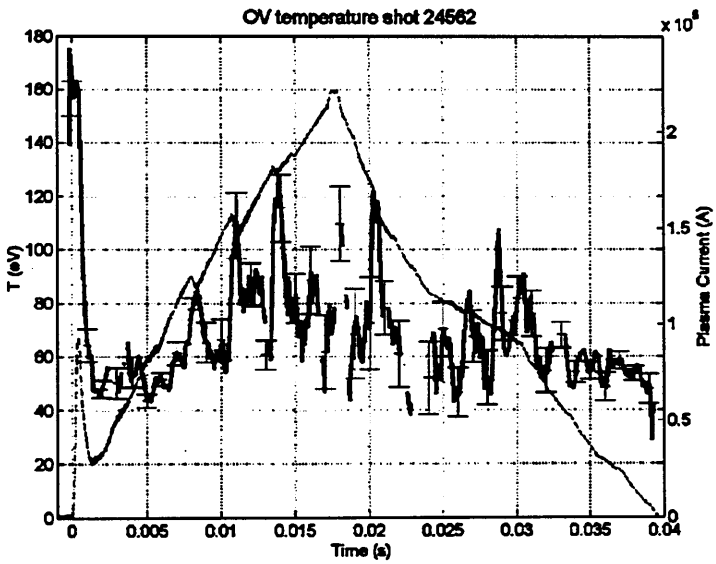

Figure 2.8: OV temperature during a CHI-initiated transformer-driven discharge. IRE's occur during the transformer driven phase at $t = 0.008$, 0.011, and 0.014 s and are accompanied by sudden increases T_i.

off, and the transformer ramp begins. The peak current in this discharge is 222 kA, and the current peak during the initial CHI pulse is 93 kA. The response time for this measurement is 560 μs, and the spectrometer is viewing along a tangential chord with an impact parameter of 0.13 m.

2.1.4 TST-2 experiments

IREs in TST-2 involve increases of plasma current as in START. Detailed explanations of experimental setup and main plasma parameters are given in Chap. 3. Analyses in terms of profile evolution and mode structure were performed using the SXR tangential camera in [51]. The decrease of SXR intensity starts from near the core of the plasma (ρ =0.3) after the growth of an $n = 1$ mode. Similarly to HIT-II experiments, increases of T_i (CIII, CV and OV) have been observed at three spatial points [52]. Fig. 2.9 shows a time evolution of T_i at different spatial positions. Note that four traces

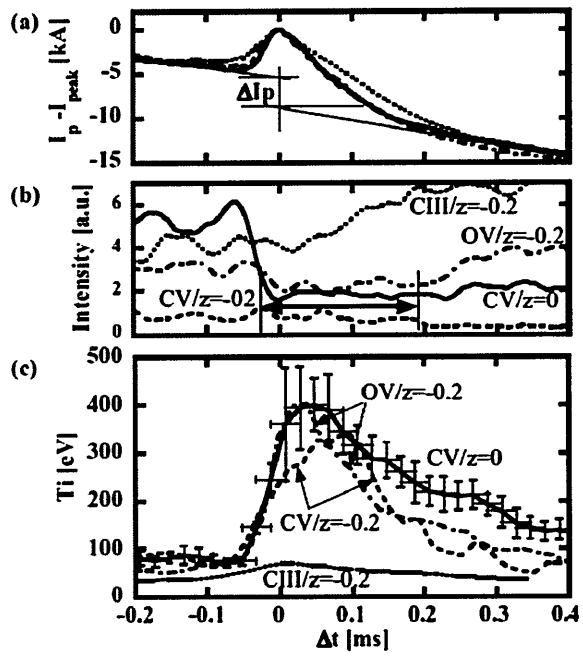

Figure 2.9: Time evolutions of the I_p (a), the intensities (b) and the temperatures of CV at $z = 0$, CV at $z = -0.2$, OV at $z = -0.2$ and CIII at $z = -0.2$ during an IRE [52].

from different discharges are plotted in this figure. T_i (CV at $z = 0$ m, CV at $z = -0.2$ m, OV at $z = -0.2$ m) increased to $\sim 400\,eV$. The increase of T_i (CIII at $z = -0.2$ m) occurs the earliest but the increment is much smaller than T_i measured using other lines. During the period indicated by the arrow in Fig. 2.9(b), the CV intensity profile became flatter and T_i reflects the information of a broad region ($\rho < 0.6$). At $\Delta t > 0.2$ ms, the CV intensity at $z = 0.2$ m decreases and the profile becomes peaked

again. Therefore, the decay of the CV intensity at $z = 0\,\mathrm{m}$ reflects the core information. Unfortunately, there is no comparison between T_i and detailed pressure or temperature profile with sufficient spatial resolution.

2.1.5 Three dimensional resistive MHD simulation of IRE

Several key features of IRE has been reproduced successfully by three dimensional MHD simulation performed by Hayashi and Mizuguchi et al. [53][54][55], and physical mechanisms were revealed theoretically. The simulation uses a full set of resistive and compressible MHD equations, which includes viscosity (spatially uniform), Ohimic and viscous heating, and local conservation of energy. The full toroidal geometry of START was used. The boundary condition is a perfect-conducting and no-slip wall at all boundaries of the computation region. The computation boundaries were typically far away from the plasma boundary in the simulation, representing experimental conditions in START and MAST. The following equations were solved.

$$\frac{\partial \rho}{\partial t} = -\nabla \cdot (\rho \mathbf{v}), \tag{2.1}$$

$$\frac{\partial \rho}{\partial t} = -\nabla \cdot (\rho \mathbf{v}\mathbf{v}) - \nabla p + \mathbf{j} \times \mathbf{B} + \mu \left(\nabla^2 \mathbf{v} + \frac{1}{3} \nabla (\nabla \cdot \mathbf{v}) \right), \tag{2.2}$$

$$\frac{\partial \mathbf{B}}{\partial t} = -\nabla \times \mathbf{E}, \tag{2.3}$$

$$\frac{\partial p}{\partial t} = -\nabla \cdot (p\mathbf{v}) - (\gamma - 1)(p \nabla \cdot \mathbf{v} + \eta \mathbf{j}^2 + \Phi), \tag{2.4}$$

$$\mathbf{j} = \nabla \times \mathbf{B}, \tag{2.5}$$

$$\mathbf{E} = -v \times \mathbf{B} + \eta \mathbf{j}, \tag{2.6}$$

$$\Phi = 2\mu \left(e_{ij} e_{ij} - \frac{1}{3} (\nabla \cdot \mathbf{v})^2 \right), \tag{2.7}$$

$$e_{ij} = \frac{1}{2} \left(\frac{\partial v_i}{\partial x_j} + \frac{\partial v_j}{\partial x_i} \right), \tag{2.8}$$

where ρ is the mass density, $\mathbf{v}$ is the velocity, $\mathbf{B}$ is the magnetic field, and p is the plasma pressure, respectively. The equations contain the resistivity η and the viscosity μ as uniform constants. The ratio of specific heats γ is 5/3. Eqs. (2.1) and (2.2) are equation of continuity and equation of motion, respectively. Eqs. (2.3) and (2.5) are Maxwell equations. Eq. (2.4) is the adiabatic equation.

The simulation starts from a linearly unstable configuration which causes initial infinitesimal perturbations to grow spontaneously. The perturbation

is introduced on the plasma velocity field at $t = 0$ as a random white noise. Figure 2.10 shows time evolutions of different toroidal mode components for various plasma parameters. The time (horizontal) axis is normalized by the

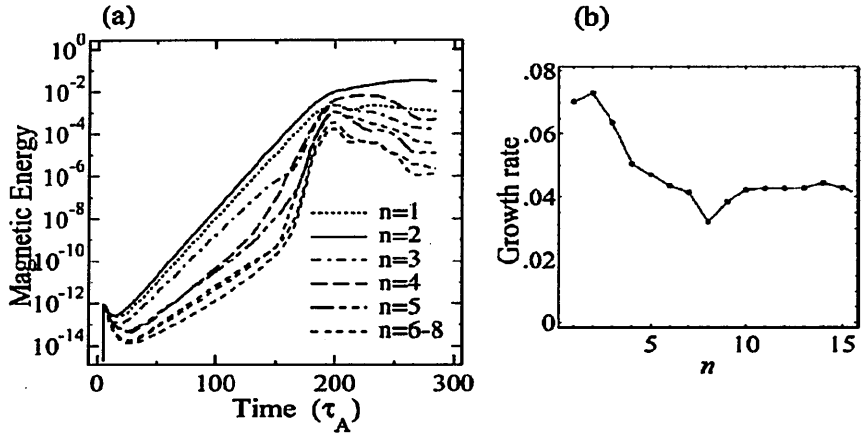

Figure 2.10: (a) Time evolution of magnetic energy for each toroidal mode n in simulation. (b) Growth rate of linear instability for each toroidal mode.

Alfven time (τ_A). There are two types of growth. The first is linear growth phase. In particular, magnetic powers for low toroidal mode numbers such as $n = 1$–3 show significant growth. The mode configurations are shown in Ref. [53]. From the poloidal mode structures shown in Fig.2.11, it is clear that the dominant poloidal modes are $m = 1$ (for $n = 1$) and $m = 2$ (for $n = 2$) modes. The color indicates the amplitude of fluctuation in plasma pressure. The position where the fluctuation is strong is the $q = 1$ resonant surface. The flow patterns are also shown by arrows in Fig. 2.11. It can be seen that m pairs of vortices are formed in the poloidal cross section. In this calculation, the source of mode growth can be determined using the energy principle. The kink and interchange terms of the potential energy integral (dW) can be expressed as

$$\delta W_{kink} = \frac{1}{2}\int d^3x \left(\frac{\mathbf{j_0}\cdot\mathbf{B_0}}{|B_0^2|}\times\xi\cdot\tilde{\mathbf{B}}\right) \tag{2.9}$$

$$\delta W_{interchange} = \int d^3x\,((\xi\cdot\nabla \mathbf{p_0})(\xi\cdot\kappa)) \tag{2.10}$$

where ξ, κ, and $\tilde{\mathbf{B}}$ denote the displacement vector, the normal curvature of the equilibrium magnetic field, and the perturbed magnetic field, respectively. Substituting the eigenfunction obtained by the simulation for ξ, these

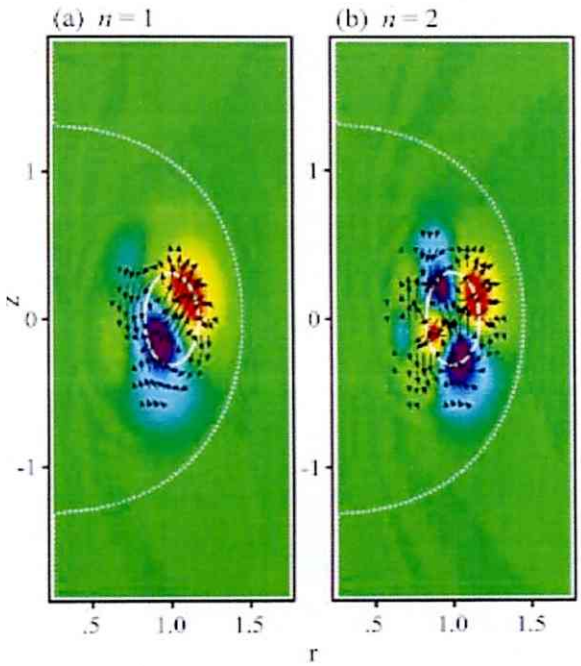

Figure 2.11: Eigenfunctions of linearly unstable modes (a) $n = 1$ and (b) $n = 2$ [53]. The color shades indicate the amplitude of fluctuation in pressure. The arrows indicate plasma flow. The location of the separatrix and the $q = 1$ rational surface are denoted by dotted and solid curves, respectively.

terms can be calculated. A negative value of δW indicates instability. The interchange term is greater than the kink term by a factor of -6.6 (for $n = 1$) and -15.3 (for $n = 2$). Therefore these modes have the characteristics of the pressure-driven mode.

During the non-linear phase, modes with high toroidal mode numbers show sudden growths as shown in Fig.2.10. For example, the magnetic energy of the $n = 4$ mode grows at $\tau_A \sim 150$ in Fig. 2.10 (a). It is caused by the development of higher harmonics for the $n = 2$ mode and by the nonlinear coupling between the $n = 1$ and $n = 3$ modes. In order to understand the mechanism they executed a simulation in which the toroidal phase of the $n = 1$ mode is initially shifted from that of the $n = 2$ mode. Figure 2.12 shows phase alignment, indicating an example of coupling between the $n = 1$ and $n = 2$ modes. The $n = 2$ mode never changes direction, while the $n = 1$ mode is split into two components and the outer one rotates spontaneously until it has aligned with the $n = 2$ mode. In this way, a localized deformation always appears in spite of the initial discrepancy in phase. In the early nonlinear stage, other high n modes are also excited in a similar way. The growths of these nonlinear modes are so rapid that the fluctuation levels soon become large enough to affect the global configuration. On the other hand, the growth rates of low n modes ($n = 1$ and $n = 2$) are saturated at around $t \sim 190\tau_A$. The time evolution of the pressure profile is shown in Fig. 2.13. Figure 2.13 (b) shows the beginning of the non-linear phase, indicating a small defomation in the plasma core. After that the deformation develops into a large bulge shown in Figs. 2.13 (c), (d). The plasma pressure in the core region is transported to the edge on a short time scale. In the early non-linear phase it is like an internal mode, but in the non-linear phase, it changes to an external mode. Such a large localized deformation of the plasma leads a local steepening of the pressure profile. Due to this increase in the pressure gradient, high-n pressure-driven modes appear and grow, resulting in reconnection of the internal and external magnetic field lines as illustrated in Fig. 2.14. Once reconnection occurs, plasma (both heat and particles) is expelled from the core to the periphery along the reconnected field line, which is much faster than radial diffusion, resulting in a rapid energy exhaust. They also studied parameter dependences of time evolution for toroidal modes like Fig. 2.10. There are three different cases: high-β cases at $q_0 = 0.91$ (< 1) (Case 1) and $q_0 = 1.05$ (> 1) (Case 2), and a low-β case at $q_0 > 1$. Case 1 is a high-β case with $q_0 < 1$. It shows linear growths of low-n modes, non-linear coupling, and rapid growths of high-n modes. Case 2 is a high-β case with $q_0 > 1$, showing slow linear growths of high-n modes. Case 3 shows slow linear growths of low-n modes, non-linear coupling, and rapid growths of low-n modes. Such parameter dependences affect the measured modes in

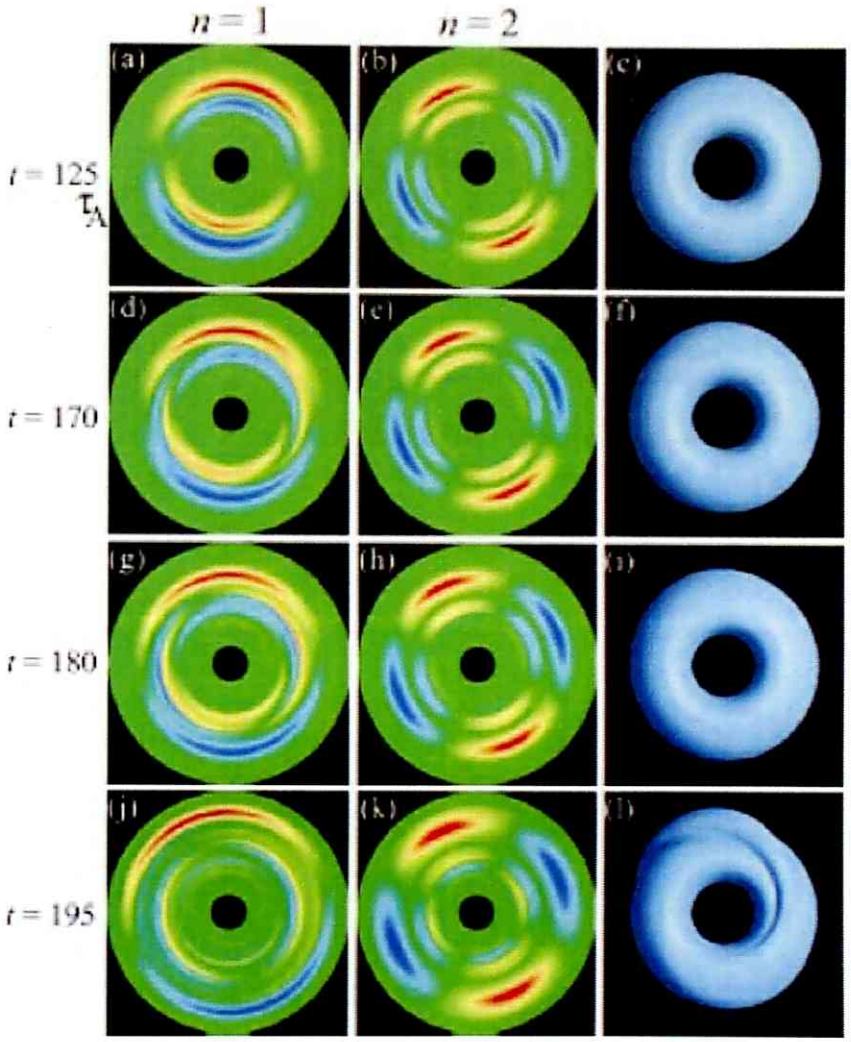

Figure 2.12: Spontaneous phase alignment between $n = 1$ and $n = 2$ modes. The temporal change in pressure fluctuation on the mid-plane for $n = 1$ (left column) and $n = 2$ (centre column) are shown by colored shades. Corresponding changes in the overall shape is shown in the right column as the top view of an iso-contour surface of the net pressure. The $n = 1$ mode rotates gradually until it is aligned with the $n = 2$ mode. The localized deformation appears at the top of the figure [53].

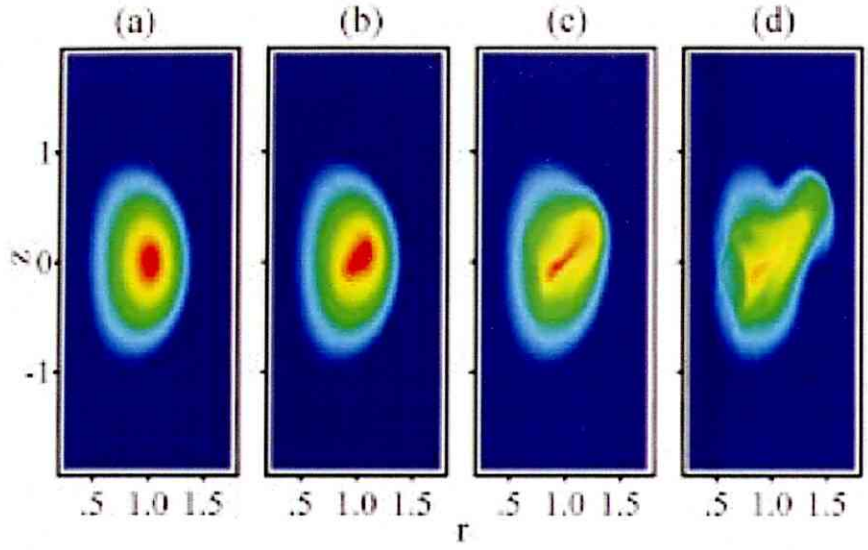

Figure 2.13: Time evolution of the pressure profile in the poloidal cross section at (a)$t = 0$, (b)$t = 165\tau_A$, (c)$t = 185\tau_A$ and (d)$t = 200\tau_A$.

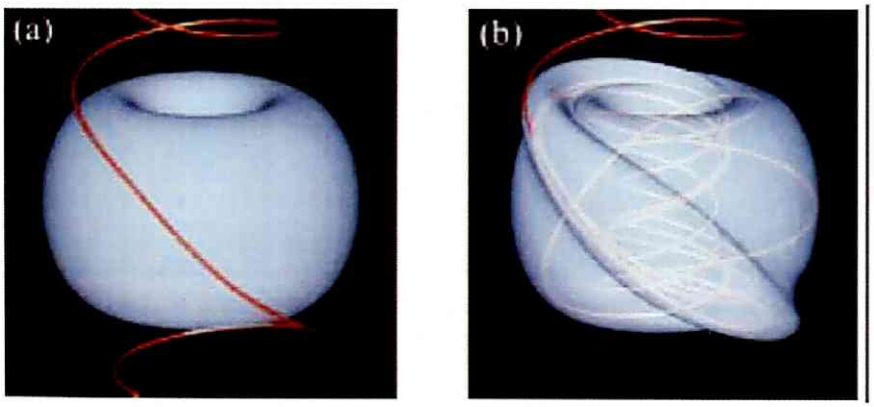

Figure 2.14: Magnetic reconnection between internal and external field lines. An identical magnetic field line and an iso-pressure surface near the separatrix are drawn for (a) $t = 0$ and (b) $t = 195\tau_A$. The magnetic field line is traced from a fixed point on the top boundary, and connects into the torus directly at $t = 195\tau_A$.

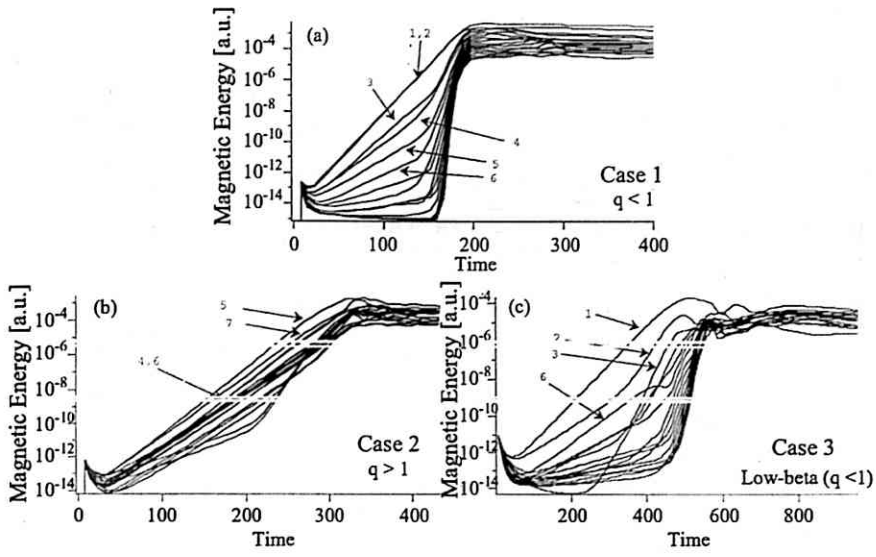

Figure 2.15: Growth of magnetic energy for each toroidal mode n. (a): Case 1: high-beta ($\beta_t \sim 10\%$) with $q_0 < 1$, (b) Case 2: high-beta ($\beta_t \sim 10\%$) with $q_0 > 1$, (c) Case 3: low-beta ($\beta_t < 10\%$) with $q_0 < 1$

the experiments.

2.2 Ballooning mode

The results of simulation described in the previous section showed that the instability responsible for IRE is pressure driven. Pressure driven modes have been observed experimentally in conventional tokamaks. The ballooning mode observed in TFTR [56] is an example of pressure driven mode. They employed an electron cyclotron emission (ECE) system, Mirnov coils and soft X-ray cameras in order to measure fluctuations in the electron temperature, magnetic field, and SXR profile [57][58]. Time evolutions of various data in a discharge with the ballooning mode are shown in Fig. 2.16. This is a typical example of the β collapse during high β_p operation. The decrease of β_p is observed in the top frame. Decreases in the SXR intensity and the electron temperature (T_e) are also observed. High-frequency modes are observed at $t = 3.77952\,s$. After the collapse, magnetic fluctuations shows large amplitude oscillations. In order to determine the mode structure, contour plots of SXR, fluctuating part of T_e and T_e are shown in Fig. 2.17. A high frequency mode with $n = 6$ appears at $t^* = 0.3\,\mathrm{ms}$ on SXR and T_e profiles.

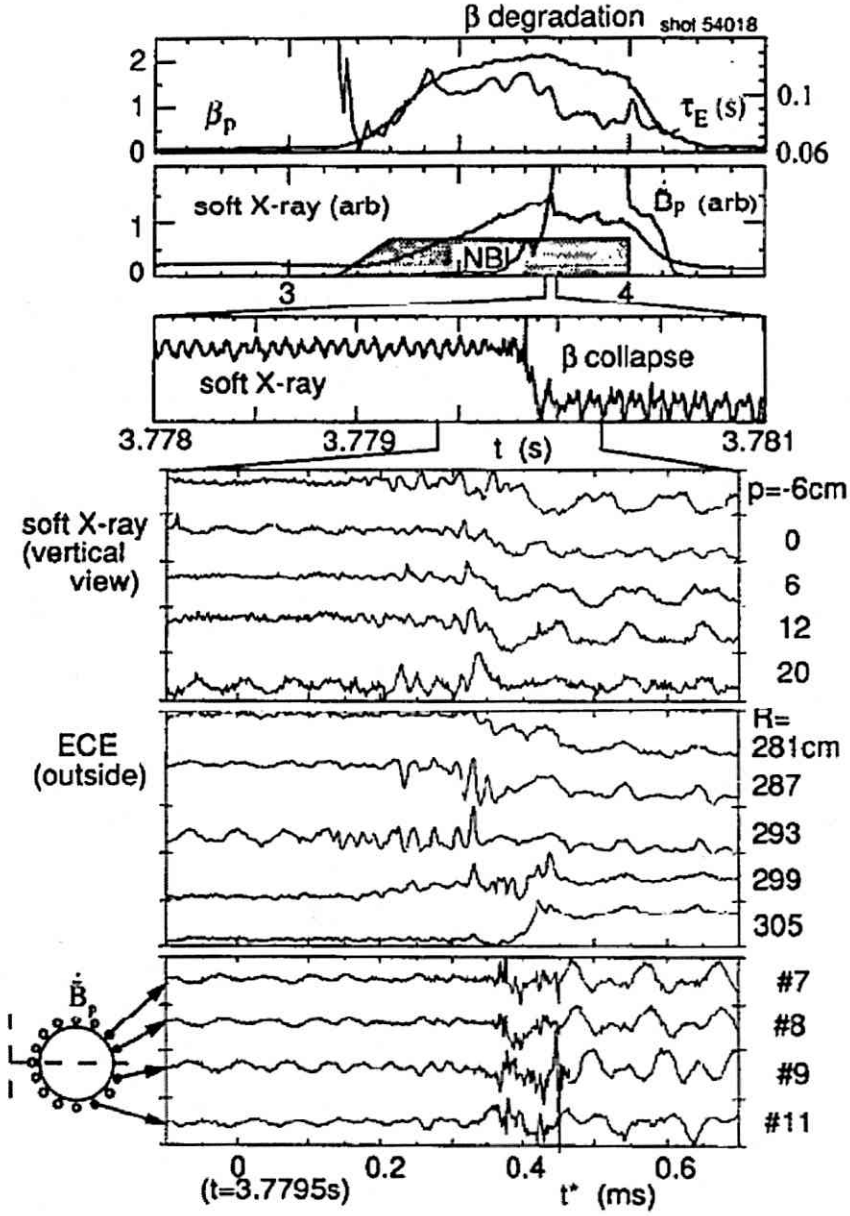

Figure 2.16: Time evolutions of various data in a high β_p plasma with a β collapse. In the bottom three frames, time is defined relative to $t = 3.7795$ s. In the soft x-ray signals, p is the chord radius [59] from the magnetic axis ($R = 2.71$ m). Negative p indicates that the sightline passes through the high toroidal field side of the plasma.

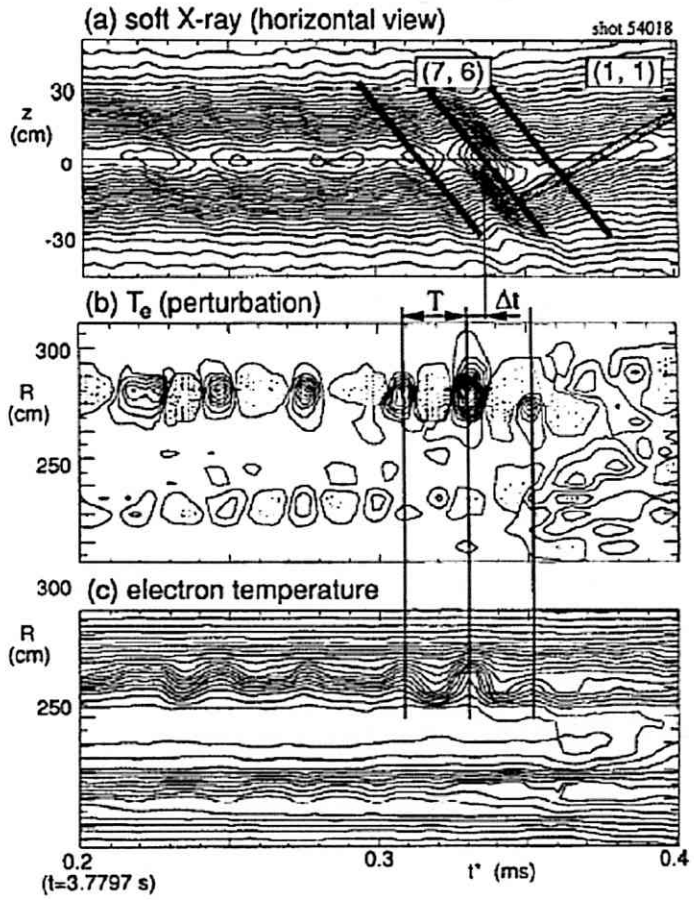

Figure 2.17: Contour plots of time evolutions of SXR and ECE profiles for shot 54018: (a) SXR profile (horizontal view), (b) electron temperature perturbation, (c) electron temperature profile. The step size of contours is 300 eV. The period of the ballooning mode is $T = 21.4\,\mu$s.

The toroidal mode number is identified by the phase difference between the SXR camera and ECE signals located at different toroidal angles. This mode has a growth time of less than 20 μs and shows a strong inside/outside asymmetry with a larger amplitude on the low field side, as is expected for the ballooning mode.

2.3 Summary of review

IREs observed on START, NSTX, HIT-II and TST-2 limit plasma performance. The time evolutions of plasma parameters including the plasma shape are discussed extensively. However detailed mode analyses and discussions of prevention of IRE are deficient. Precursors are usually low-n modes. ($n = 1$ on START, NSTX and TST-2).

Characteristics of IRE were reprocuded by three dimensional resistive MHD simulation performed by Hayashi, Mizuguchi et al. There are linear and non-linear phases of growth for each toroidal mode. A non-linear mode coupling between $n = 1$ and $n = 2$ modes leads to phase alignment, which resuts in a larger localized deformation of the plasma and a local steepening of the pressure profile. The increased pressure gradient drives high-n pressure-driven modes unstable, resulting in reconnection of internal and external magnetic field lines. Once reconnection occurs, plasma is expelled quickly from the core to the periphery along the reconnected field lines, since parallel flow is much faster than radial diffusion.

The existence of other precursors induced by non-linear coupling, predicted by Hayashi, Mizuguchi, et al. has not been discussed or discovered. One reason is the difficulty due to asymmetric configuration of the magnetic field in ST. We need a way to understand the mode structure, especially in the poloidal direction. Understanding of the drive mechanism of IRE is essential for its prevention. In a conventional tokamak such as TFTR, identification of instability as a pressure driven ballooning mode with high-n was made.. The mode was localized on the outboard side (bad curvature region) with a steep temperature gradient.

An increase of the ion temperature is observed in TST-2 and HIT-II. Both experiments measured the ion temperature from Doppler broadening of impurity line emission. In HIT-II a rapid increase in T_i (OV) of 50–75 eV from the usual T_i of 50-0100 eV. In TST-2 significant increases of T_i (OV and CV) from 100 eV to 300–500 eV are observed. And they succeeded in measuring the profile with two spatial points and by comparison with the SXR intensity profile. However time evolution of the profile with sufficient spatial resolution has not been discussed.

In tokamak experiments including STs, ELMy H-modes are often observed. The ELM is classified into more than three types (See Sec. 1.2.9). The sawtooth oscillation (Sec. 1.2.7) is an MHD instability which is localized in the core of the plasma ($q \sim 1$). However, there is no clear classification and definition of IRE, ELM and sawtooth. Mode analysis, profile analysis, and characterization of collapse are keys for classification.

2.4 Significance of studying MHD instability

The final goal of MHD instability studies is to realize instability-free plasmas for stable operation of fusion reactors. There are two steps to this goal. First we need to understand the mechanism of instability. In particular, critical questions are "which modes become unstable, how they grow, and how is the plasma collapse triggered?" Once we understand the mechanism, it becomes possible to suggest mthods for prevention. The second step is to demonstrate such suggested methods in real experiments. In this thesis, the focus is on the first step for obtaining IRE-free ST plasmas. IRE limits plasma performance. In MAST, IRE causes an H to L transition, or in the worst case plasma disruption. H-mode is the standard operating mode in ITER, and most probably for an ST reactor. These are the reasons that this study is very important in fusion research.

2.5 Objective of this study

IREs involve magnetic reconnection and limit plasma performance in many experiments. In this study, IRE is treated as a instability with mode coupling and/or accompanied by a collapse at a rational surface except for the $q = 1$ surface.

The 3-D MHD simulation performed by Hayashi, Mizuguchi, et al. showed non-linear growths of pressure driven modes. However, how precursor modes couple to each other and how such modes destroy the plasma profile are not understood experimentally so far, and the predicted unstable mode has not been confirmed experimentally as pressure driven. Understanding of the mode behaviour is the main objective of this study.

Ion temperature increase is very important for understanding the fundamental physics of magnetic reconnection, because the acceleration mechanism is uncertain. A comparison between the time evolutions of ion temperature and SXR profile with sufficient temporal and spatial resolutions may contribute to the understanding of spatial diffusion of accelerated ions and

fundamental reconnection physics.

Moreover, clear classification and differentiation of sawtooth oscillation, ELM and IRE have not been done. Summarizing these instabilities contributes to the understanding of stability of ST plasmas.

The objectives of this thesis are:

1. To identify mode numbers of IRE precursors in the unique configuration of ST.

2. To determine whether or not non-linear coupling and/or multiple modes, predicted by MHD simulation, exist during IRE .

3. To confirm whether or not a pressure driven mode exists as a precursor of IRE.

4. To find the trigger condition for IRE and a way to avoid IRE.

5. To compare time evolutions of the SXR profile and T_i increase in order to understand the fundamental reconnection mechanism.

6. To find and summarize the differences among IRE, ELM and sawtooth oscillation in ST.

Chapter 3

Experimental setup for TST-2

3.1 Tokyo spherical tokamak-2 (TST-2)

TST-2(Tokyo Spherical Tokamak-2) is a spherical tokamak in Japan (kashiwa campas at in the university of Tokyo)[60]. TST-2 was moved to Kashiwa Campus from Kyushu University due to a collaboration in 2004, and restarted experiments in 2005. Main parameters of TST-2 are summarized in Table 3.1.

There are three types of coils in TST-2 as shown in Fig. 3.1. The OH coil

parameter	value
Major radius R	$\sim$ 0.38 m
Minor radius a	$\sim$ 0.25 m
Aspect ratio A	$\sim$ 1.5
Toroidal magnetic field B_t	$\sim$ 0.3 T
Plasma current I_p	$\sim$ 0.1 MA
Discharge time	$\sim$ 10 ms

Table 3.1: Typical parameters of TST-2.

which induces toroidal electric field to drive the plasma current is set at the centre of torus. The plasma current produces the poloidal magnetic field necessary for plasma confinement and heats the plasma resistively. The TF coils produce the toroidal magnetic field needed for stability. The poloidal field coils provide necessary fields for plasma position and shaping control. PF3 coil provides the main vertical field to control the horizontal position, Whereas H coil provides the horizontal field to control the vertical position. PF2 and PF5 coils are used to adjust the poloidal field configuration. A photograph of TST-2 is shown in Fig. 3.2. There are, mainly, three different

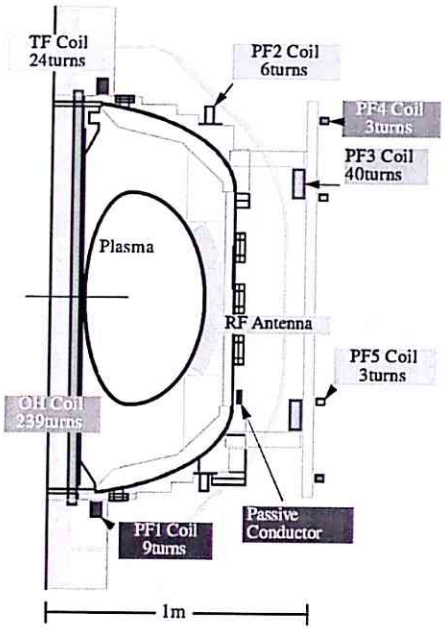

Figure 3.1: Locations of coils in TST-2.

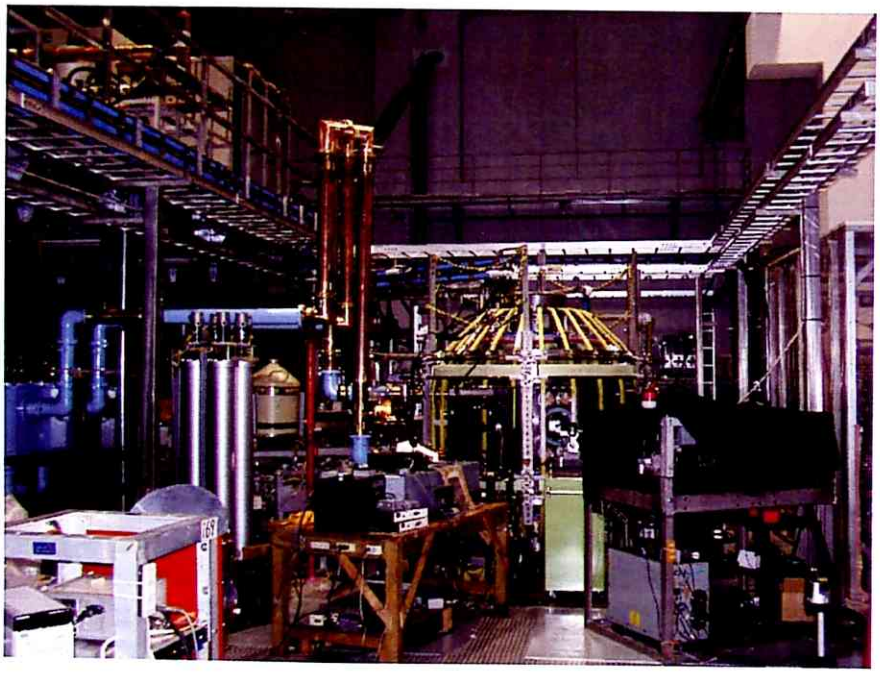

Figure 3.2: TST-2 spherical tokamak.

types of experiments.
1: Plasma heating experiments using high harmonic fast wave (HHFW).
The effectiveness of HHFW for electron heating has been studied in high-β and low magnetic field configuration[61][62]. 400 kW of injection power using HHFW at 21 MHz is available for additional heating of plasma. Increase of radiation from the plasma with high energy photon (< 1 keV) has been observed during the injection, suggesting electron heating. The radiation was measured by the SBD (surface barrier diode) array with 5 channels which are photo diode with Beryllium filter (7μm)[51]. Electron temperature (T_e) can be measured by a compact Nd:YAG laser Thomson scattering system. An electron temperature increase from 140 eV to 210 eV was observed upon injection of 200 kW of RF power[63]. However, there is one problem about the effectiveness of the heating. Parametric decay instability (PDI) and the scattering of the HHFW can affect both propagation and heating. Such characteristics has been studied by using magnetic probes and visible light fluctuations[64].
2: Start-up experiments using electron cyclotron heating and the HHFW
Recently, various scenario for effective methods of plasma start-up has been studied. Because removing center solenoid coil (Ohmic coil) is essential in order to realize spherical tokamak reactor. A spherical tokamak reactor has low aspect-ratio plasma and no room for Ohmic coil. On TST-2, a magnetron (2.45GHz/5kW) and a horn antenna were used to inject electron cyclotron (EC) wave (either O-mode or X-mode)[66]. The experiments were performed and various parameter and configuration dependences were studied. There is no clear difference between O-mode and X-mode injection in terms of achieved plasma current, discharge waveforms and parameter dependences. In many discharges, clear current jumps has been observed, and it was found that the current ramp-up rate before the jump is very important. The ramp-up rate increases with the injected ECH power, and decreases with B_z, filling pressure and B_t. The B_z was generated by the PF coils. These results suggest that high energy electron confinement is playing an important role. Sustainment using HHFW (10-24 kW) has also observed in ECH start-up discharges[67][68]. The current jump induced by the only ECH, can be induced earlier by the RF heating, and a constant plasma current was sustained even after the ECH power was turned off. The maximum sustainment time by the RF power alone was 40 ms, limited by the RF pulse length. Figure 3.3 shows one example of a discharge with the sustainment which is shown in [67]. The plasma currents (Fig. 3.3(a)) reaches $\sim$1 kA in the discharged by the HHFW (blue broken line) . There are some increase of line integrated electron density measured interferometer during the current jump-up phase in both cases(Fig. 3.3(b)). H_α/D_α seems to increase much

more by RF power injection, suggesting high recycling at the RF antenna. (Fig. 3.3(c)). Fig. 3.3(e) shows the injected ECH and HHFW power.

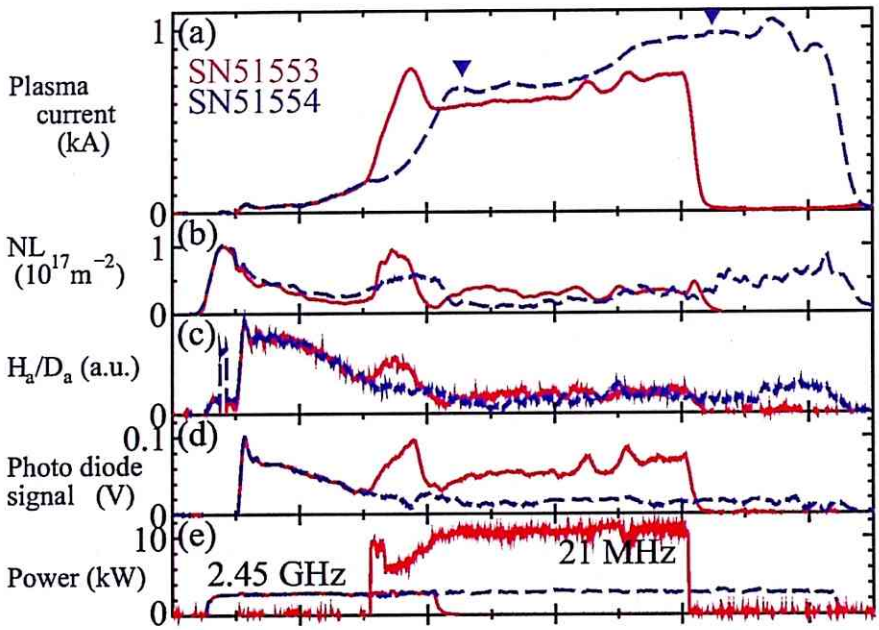

Figure 3.3: Two discharge waveforms (red solid lines for RF sustained plasma and blue dashed lines for ECH sustained plasma); the plasma current (a), line integrated electron density (b), H_α/D_α emisssion (c), radiation from visible to soft X-ray (d), and ECH and RF net powers (e). Additional gas puffing to the ECH sustained plasma is marked by trigonal symbols in (a).

3. Studies about MHD events
Due to MHD instability, the plasma sometimes have minor disruption. The behavior has been studied by the soft X-ray radiation (SXR) profile in [51][52]. From next chapter, the detailed measurements of SXR and ion temperature by the spectroscopy will be introduced and discussed with mode analysis.

3.2 Soft X-ray measurements

In order to understand mode behavior and profile depending on temperature and density, measurements of soft X-ray radiation (SXR) has been carried out. In this section, explanation and experimental set-up of SXR detectors are focused.

3.2.1 Introduction of semi-conductor detector for measurements of soft X-ray

Impurity-doped semi-conductor and p-n junction

Solid materials are classified into insulator, conductor and semi-conductor by electrical conductivity. No current flows in an insulator, and current proportional to the applied electric field flows in a conductor. In a semi-conductor no current flows at low temperature but current flows at high temperature. When impurities are added to a semi-conductor, its property changes. The semi-conductor acquires extra electrons or holes and the electrical conductivity increases. Si (silicon) has four valence electrons. If some Si atoms are replaced by, for example, Sb (antimony) which has five valence electrons, four valence electrons can be covalently bonded but the fifth electron cannot be bonded and is added to the conduction band. This state is called the donor state, and Sb is called a donor atom. As the electrical conductivity comes from extra electrons, such a semi-conductor is called the n-type semi-conductor (Fig. 3.4). If the added impurity is B (boron), which has only

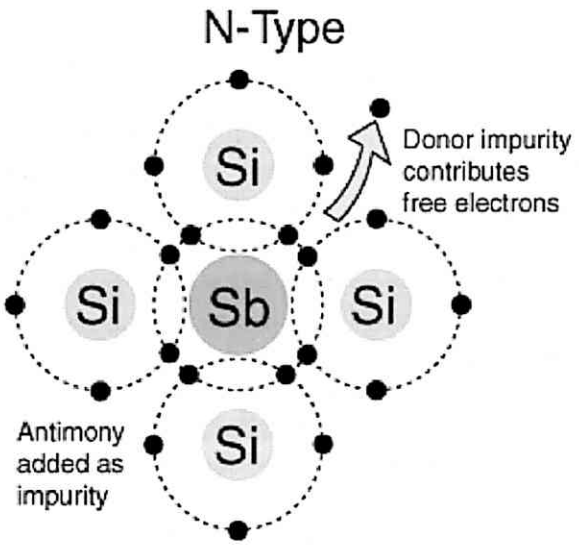

Figure 3.4: Schematic of n-type semi-conductor.

three valence electrons, there will a vacancy of electron called the hole. This state is called the acceptor state, and B is called an acceptor atom. Such a semi-conductor is called the p-type semi-conductor because the carrier (the

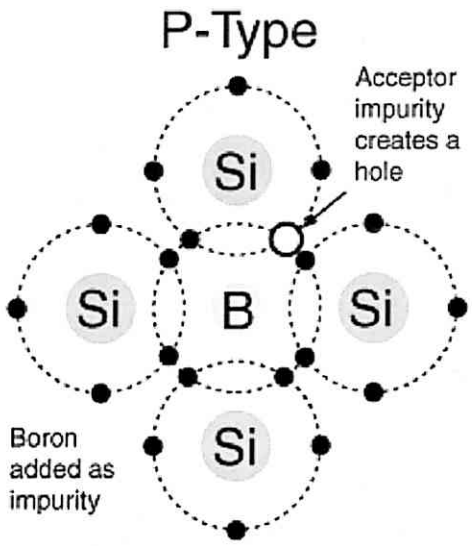

Figure 3.5: Schematic of p-type semi-conductor.

hole) has a positive charge (Fig. 3.5).

The p and n-type semi-conductors are electrically neutral. In order to detect X-ray photons, p-n junction in a semiconductor crystal, created by bonding p-type and n-type semi-conductors. is often used. The schematic of this mechanism is shown in Fig. 3.6. By diffusion some fraction of electrons and holes move to p-type and n-type regions (b). In equilibrium, it creates an electrical potential difference of V_0. When an external voltage V_b (reverse bias) is applied to add positive voltage in the n-type region, the electrical potential difference between the two electrodes is increased to $V_0 + V_b$ and prevents motion of electrons and holes (c). Under this condition, extra electrons in the n-type semi-conductor and holes in the p-type semi-conductor are concentrated near opposite electrodes. Near the junction of p- and n-type semi-conductors, a region with no extra electrons or holes, called the depletion layer, is created.

X-ray detection

The sensitive region in a p-n junction is the depletion layer. When an X-ray photon strikes the depletion layer, it makes pairs of holes and electrons. The number of hole-electron pairs is proportional to the energy of incident photon. An energy of 3.65 eV is needed to make one hole-electron pair in a

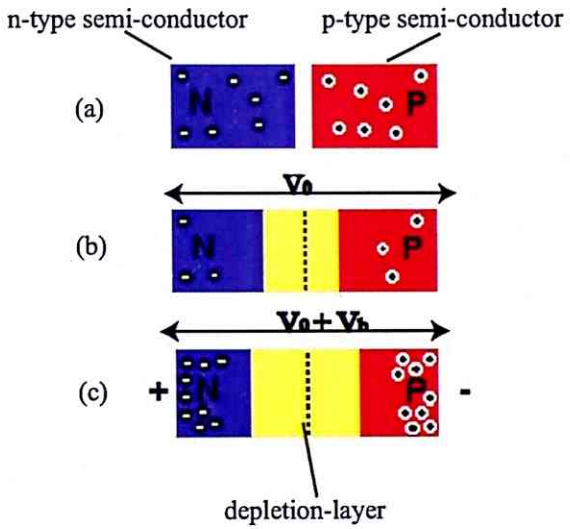

Figure 3.6: Schematic of p-n junction in a semiconductor crystal.

Si crystal. For example, considering the incidence of one photon with 3keV, the number of hole-electron pairs created is

$$\frac{3 \times 10^3[\mathrm{eV}]}{3.65[\mathrm{eV/pair}]} \sim 8.21 \times 10^2[\mathrm{pair}]. \tag{3.1}$$

The created holes and electrons move towards negative and positive electrodes, respectively and creates a current proportional to the energy of the incident X-ray photon.

3.2.2 PIN-diode array for tangential chords

Principle of operation

PIN-diode is commonly used since the depletion layer thickness can be tailored to optimize quantum efficiency and frequency response. Here, quantum efficiency is defined as the number of electron-hole pairs generated by one incident photon. Principle of operation of PIN-diode is almost the same as p-n junction. PIN diode consists of three layers, p-type region, intrinsic layer, and n-type region, as shown in Fig. 3.7. The intrinsic layer contains few impurities, and is much thicker than a normal pn-junction semi-conductor. PIN-diode must be used in vacuum, because SXR is easily stopped in air.

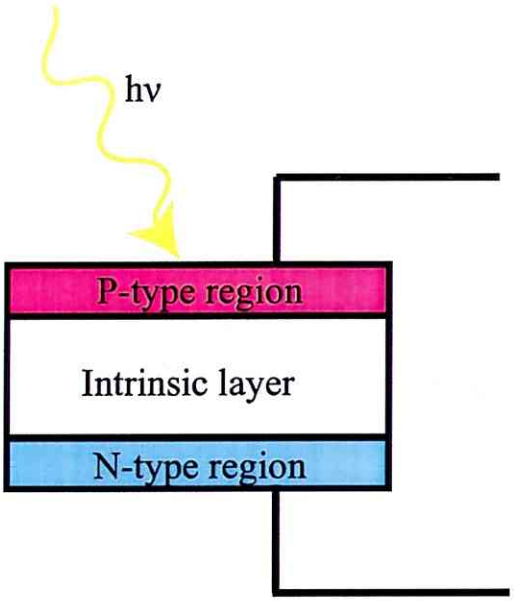

Figure 3.7: Schematic of PIN-diode.

Experimental setup

The output signal from the PIN diode itself is current with several μA. Therefore amplification is necessary for enough voltage at digitizer. To measure fluctuations of SXR in the plasma it is crucial to understand the frequency response. The frequency response including pre-amplifier was measured using a semi-conductor laser as a light source, since the intensity and modulation frequency can be controlled. The measured frequency response is shown in Fig. 3.8. This result indicates that this PIN-diode can measure fluctuations up to about 10 kHz with flat response, but the response decreases to a half at 50 kHz. The output signal from the pre-amplifier is amplified by an isolation amplifier which can separate the earth of the output signal from that of the input signal. Generally, earth of signals from detectors should be separated from potential (earth) at the vacuum vessel to prevent unexpected current to digitizers and noise. The frequency response of the isolation amplifier is measured using a function generator. The result is shown in Fig. 3.9. Relative error is about 1% up to a frequency of at least 100 kHz. A photograph of the 20-channel PIN-diode array used in this study is shown in Fig. 3.10. The size of each element is 1.5 mm$\times$12 mm, and neighboring elements are separated by 0.75 mm.[69] The PIN-diode array is mounted on a midplane port (Port-12C, $Z = 0$) and have tangentially viewing chords to measure the radial

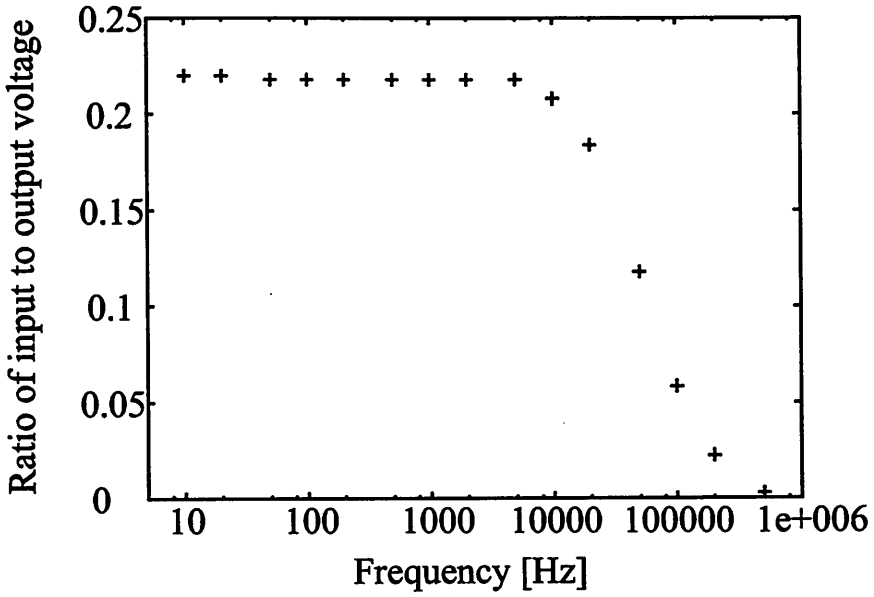

Figure 3.8: Frequency response of PIN-diode.

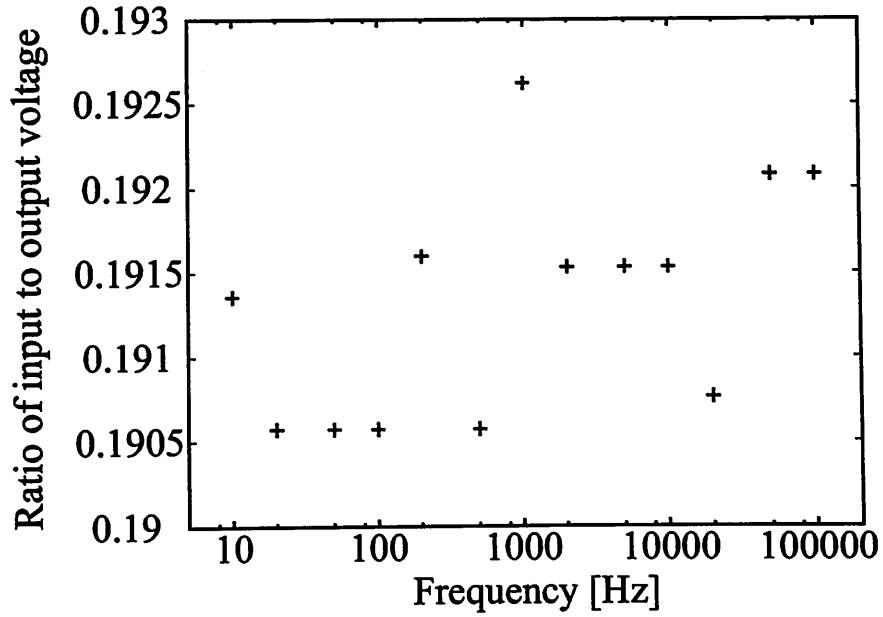

Figure 3.9: Frequency response of isolation amplifier.

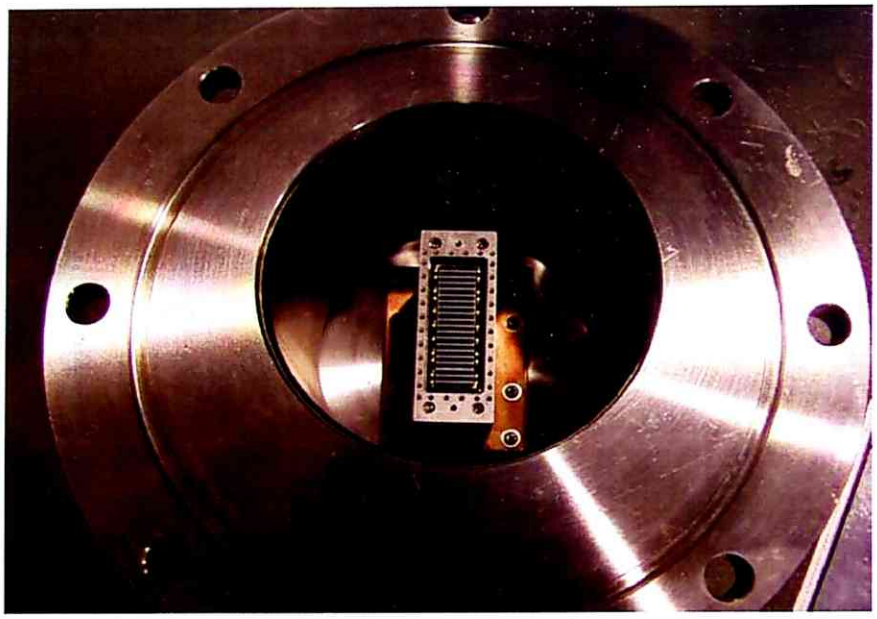

Figure 3.10: 20-channel PIN-diode array used in this study.

SXR profile as is shown in Fig. 3.11. A pinhole ($\phi = 1r, \mathrm{mm}$) was in front of the array to define the sightlines. The PIN-diode signal was amplified by isolation amplifiers and were digitized at a sampling rate upto 1 MHz.

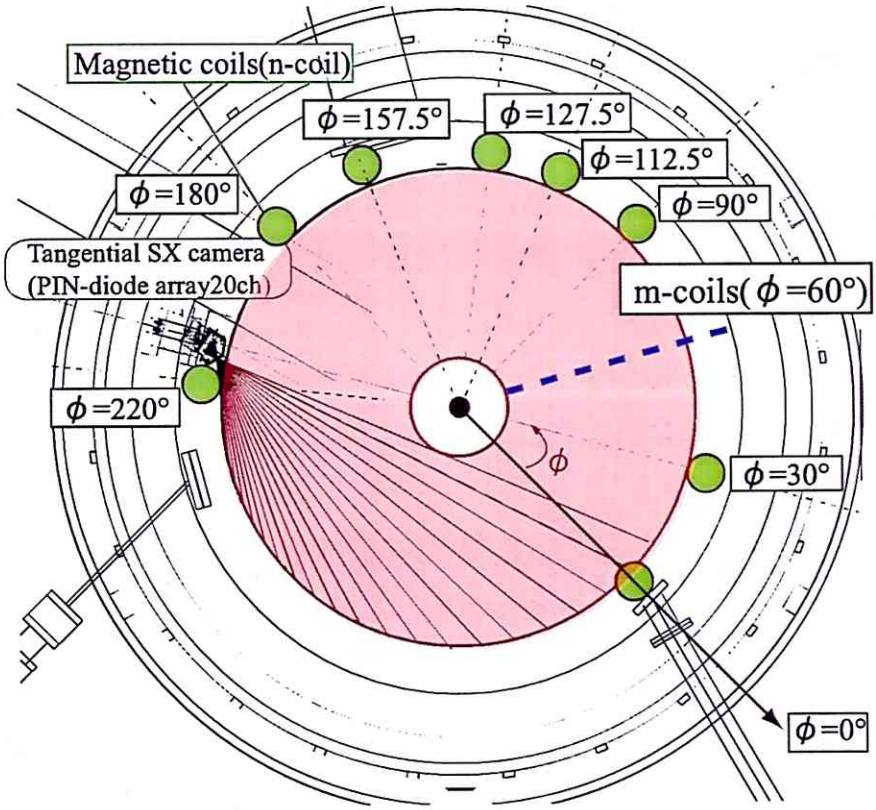

Figure 3.11: Tangentially viewing chords of the 20-channel PIN-diode array and positions of n-coils.

3.2.3 AXUV array for vertical and horizontal chords

Principle of operation

The "AXUV (Absolute UV Silicon Photodiodes) diode" [70] is a name of commodity in IRD Inc. and photo diode for measurements of radiation from plasma. These detector are employed in many plasma experiments such as DIII-D[71], TCV[72] and CHS[73]. These diodes consist of a silicon p-n junction photo diode and have been developed for applications in the vacuum ultraviolet, extreme ultraviolet and the soft x-ray (XUV,wavelength range 1800 Åto 2 Å, energy range 7 eV to 6000 eV) spectral region. Unlike common p-n junction diodes, these diodes do not have a doped dead-region and have zero surface recombination resulting in near theoretical quantum efficiencies for XUV photons and other low energy particles. The absence of a dead region yields complete collection of the photogenerated carriers by an external circuit resulting in 100% carrier collection efficiency and near theoretical quantum efficiency. For incident photons with more than ~10 eV, the quantum efficiencies from [74] shows linear with the respect to its energy in logarithmic scale as is shown in Fig. 3.12. Figure 3.13 presents the responsi-

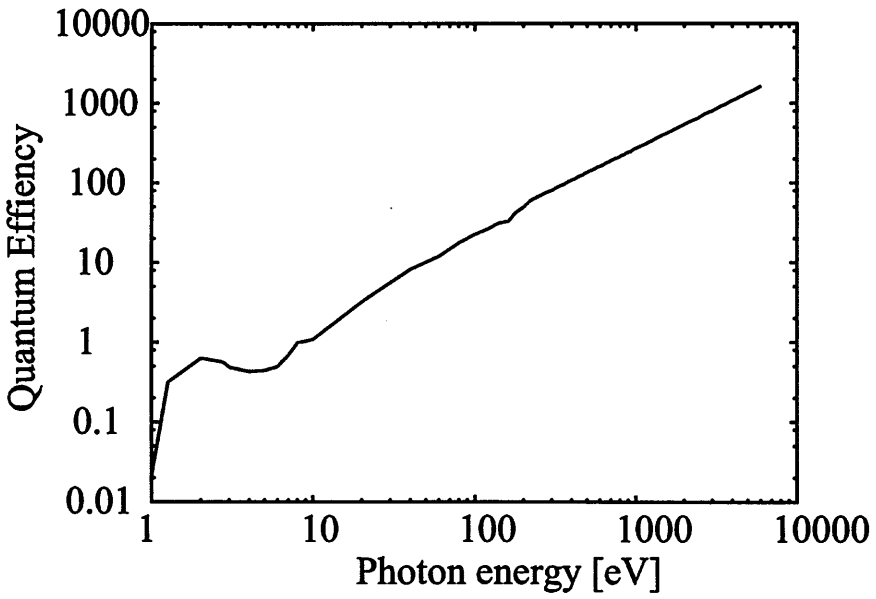

Figure 3.12: Quantum efficiency of AXUV photo diode

bility of AXUV diode. If we know the energy spectrum and its intensity of the photon from the plasma, it is possible to determine the output currents because the units of the responsibility is [A/W].

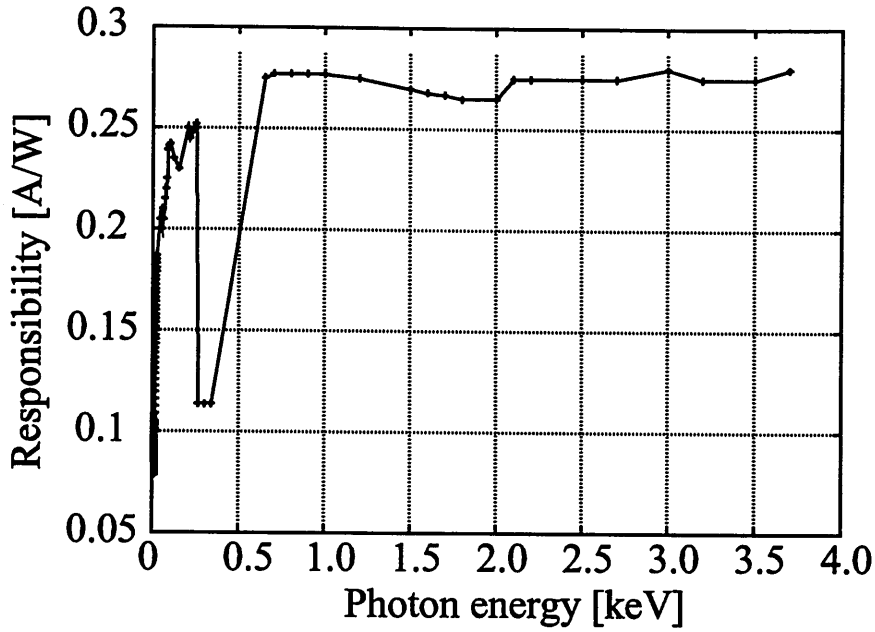

Figure 3.13: Responsibility of AXUV diode

Experimental setup

Other three detectors have been installed in TST-2 at PORT-10A, D and E. Two of them (AXUV) have vertical chords for radial profile of SXR. The other one has horizontal chords for vertical profile. Since signals from detector itself are currents, it is necessary to use pre-amplifiers and isolation amplifiers as same as the PIN diode array (tangential SXR camera).
Detectors (photo-diode) at PORT-10A and D are AXUV-20EL with 20 channels. The detector at PORT10-E is AXUV-16ELOHYB1 with pre-amplifier. The main specifications of these two detectors is shown in Table 3.2. For

	AXUV-20EL	AXUV-16ELOHYB1
Sensitive area	$3\,mm^2(\times 20)$	$10\,mm^2(\times 16)$
Size	$0.75\,mm \times 4\,mm$	$2\,mm \times 5\,mm$
Capacitance	$1\,nF$	$2\,nF$
Rise time	$0.2\,\mu s$	$0.5\,\mu s$

Table 3.2: Main specifications of AXUV-20EL and AXUV-16ELOHYB1.

AXUV-20EL, two pre-amplifier (8986A) made in CLEAR PULSE have been employed. Its substrate is made of ceramic and the cables are teflon lines to

prevent gas-emission. The main specifications is shown in Table 3.3 Cables

Input current	$< \pm 1\,\mathrm{mA}$
Input frequency	$< 500\,\mathrm{kHz}$
Output voltage	$< \pm 10\,\mathrm{V}$
Output impedance	$50\,\Omega$
Gain	$10^5\,\mathrm{V/A}$
Power supply voltage	$\pm 12\,\mathrm{V}$

Table 3.3: Main specifications of 8986A.

for output connect to a 50-pin D-sub feed-through in VG50. The overview picture of SXR cameras (pre-amplifier and cables) is shown in Fig.3.14. On

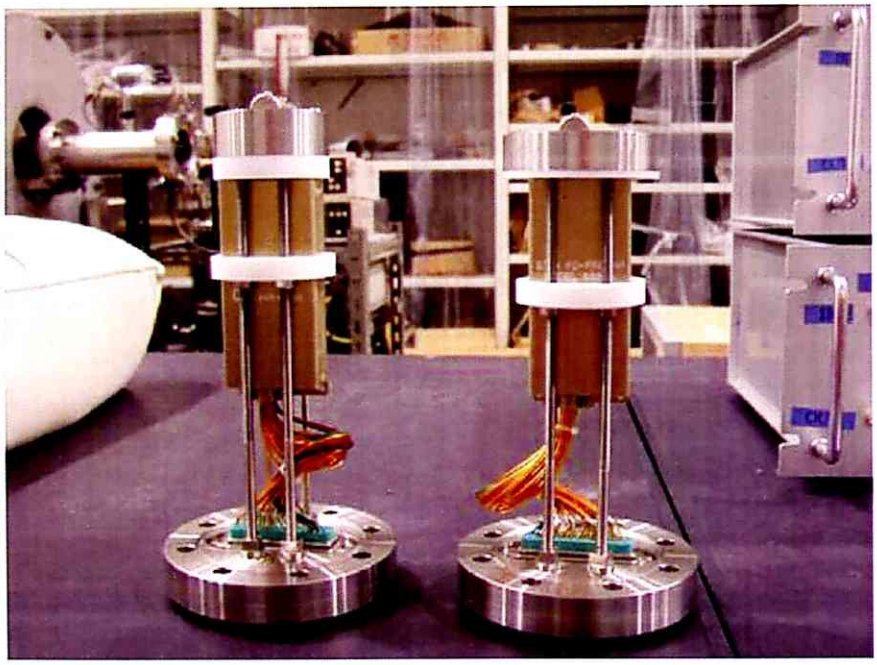

Figure 3.14: SXR camenras for horizontal and vertical chords with pre-amplifiers(8986A)

the top of the detectors, filters for cutting incident photons with low energy can be installed. In the column-shaped covers there is each detector on the top of 8986A. Photons from the plasma must go through the filters and slit in the covers. With the slit, the detectors have spatial resolution to measure the profile. The size of the slit for both detectors is $4\,mm \times 1.5\,mm$. The

frequency response of 8986A is shown in Fig. 3.15. The gain decrease with frequency and reach half value at 500 kHz. This 500 kHz is a standard for frequency response. Therefore it is enough to measure modes with high frequency in plasma. As isolation amplifier, T-ISA001 (TURTLE INDUSTRY

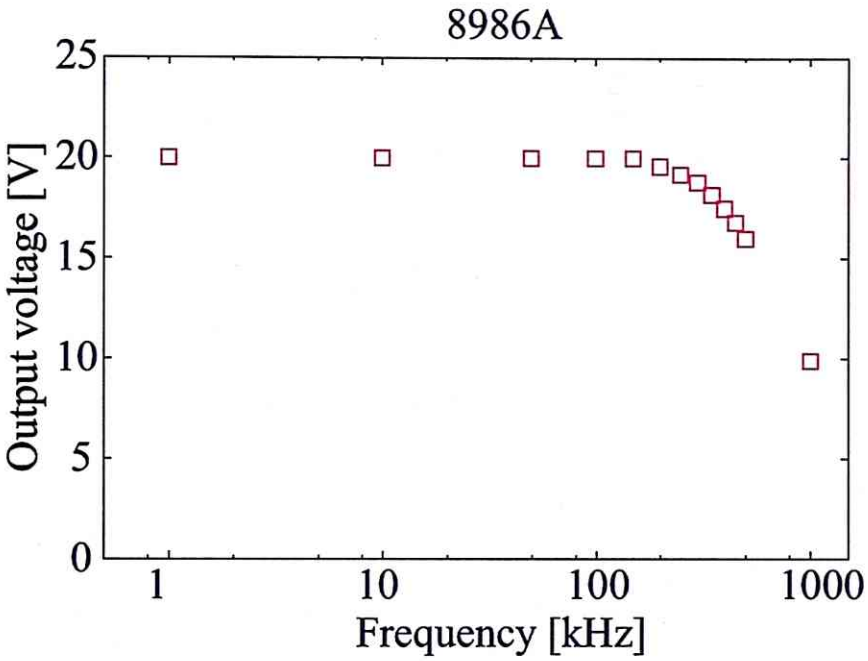

Figure 3.15: Frequency response of 8986A (CH5).

Co. Ltd.) is used. Its withstand voltage= 1500 V, input resistance = 100 kΩ, gain (V_{in}/V_{out}) = 10 (20 dB), input voltage range ~ ±1.2 Vp, output voltage range ~ 12 Vp, frequency response < 1 MHz and output resistance = 50 Ω. The detector at PORT10-E is AXUV-16ELOHYB1 with pre-amplifier. The top view of the detector is shown in Fig.3.16. The circuit of the pre-amplifier is hexagonal shaped and make it very compact. At the centre of the substrate, there is the array of sensitive region with 16 channels. The output lines connect to 48-pins feed through installed on VG40. As same as the previous two SXR cameras, a slit (1 mm × 14 mm) is in front of the detectors for enough spatial resolution. Figure 3.17 presents the frequency response from the diode to pre-amplifier which is measured by using incident modulated light (semi-conductor laser). This result is similar to previous 8986A and enough to measure the mode with at least 500 kHz. Note that the way to measure the frequency response of AXUV-16ELOHYB1 and 8986A is different. In this case the intensity of modulated light was limited by small

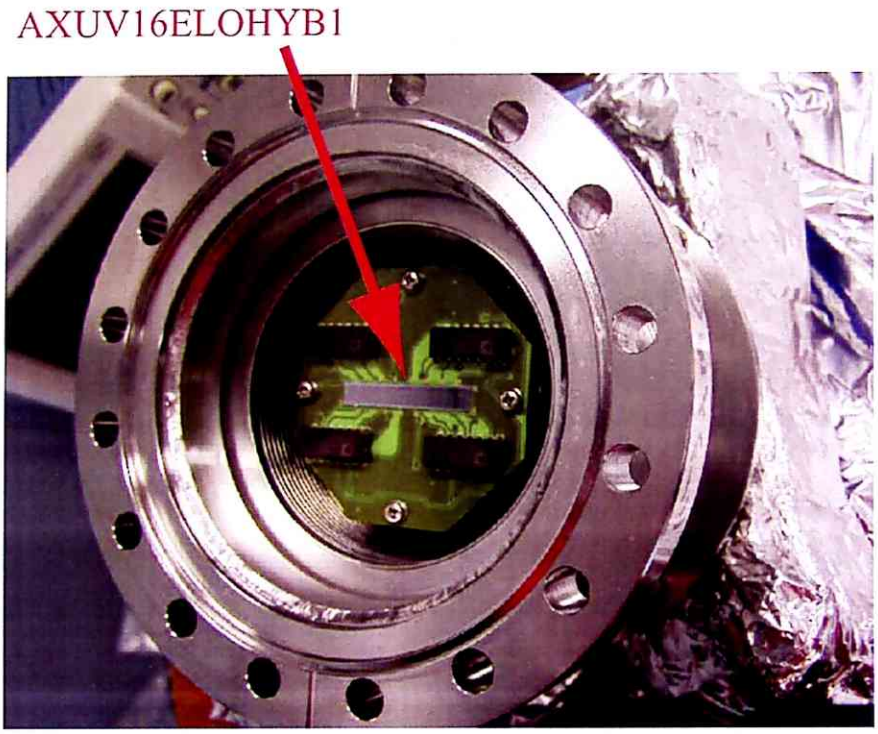

Figure 3.16: Top view of SXR camenra at PORT10-E for vertical chords (AXUV16ELOHYB1).

pin-hole. On the contrary, in the case of 8986A, the frequency response was measured by modulated current from input, directly. Therefore there is significant difference on the output voltage.

Turning now to geometric configuration of these SXR camera. When these SXR cameras are installed, confirmation of alignment is necessary. Because unexpected errors from small different position of detectors compared to ideal drafts. Therefore alignment had been done with using visible laser. Figure 3.18 presents results of alignment for SXR cameras. The laser put on position on a pole with a scale and is steered toward the slit. For SXR camera at PORT-10A, a horizontal pole was used for alignment. Fig. 3.18(a) shows the correlation between coordinates of detector and position with maximum measured signal from the laser. Note that the positions of vertical axis are corrected for radial position (R) at $Z = 0\,\mathrm{m}$ and some channels are not measured because of lack of space. (The pole was not at $Z = 0\,\mathrm{m}$) Since the correlation should be geometric, it is reasonable to do linear-fitting for other unmeasurable channels and adjust alignment results. The result of linear fitting is showed as red line. For the camera at PORT-10D (Fig. 3.18(b)), the

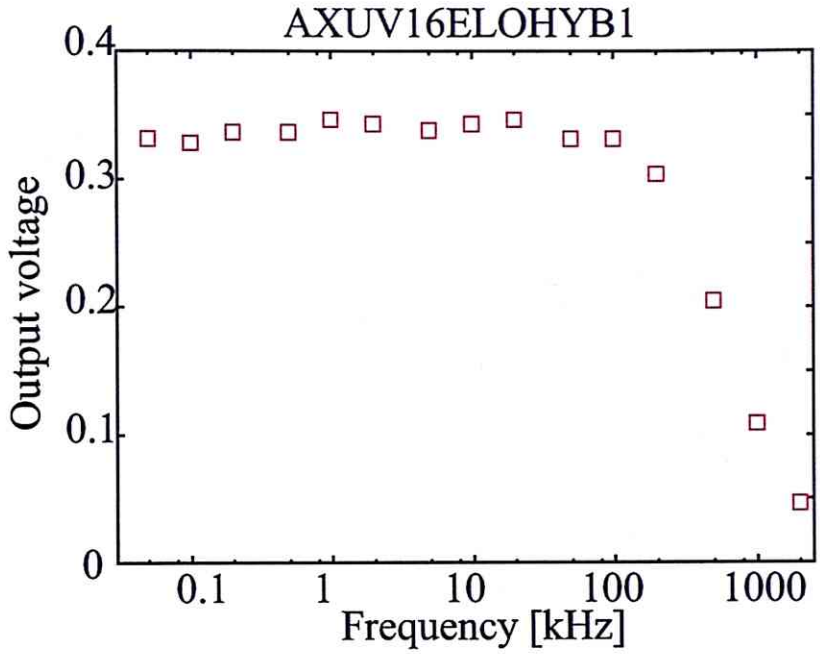

Figure 3.17: Frequency response of AXUV-16ELOHYB1 (ch8).

vertical axis is Z at $R = 0.37\,\mathrm{m}$. For the camera at PORT-10E (Fig. 3.18(c)), the vertical axis is R at $Z = 0\,\mathrm{m}$.

Generally on measurements of SXR, it is better to consider filters for limiting photons with low energy. Because mode behavior near the core of the plasma can be seen from high energy photons (SX). However, for the plasma with low temperature we sometimes do not need such filters. In the TST-2 plasma, $T_e \sim 100\,\mathrm{eV}$, therefore photons with $\sim 100\,\mathrm{eV}$ should be measured. A lot of filters are used in other tokamak experiments. However for the plasmas with $T_e > 1\,\mathrm{keV}$, thin beryllium sheet is often used for SXR measurement. These cameras can be installed three types of filters (zirconium, beryllium and polypropylene). The transmissivities of the filters with respect to energy are calculated from X-ray mass attenuation coefficients. The coefficients and transmissivity can be expressed by the following formula [75].

$$I/I_0 = \exp(-(\mu/\rho)x) \tag{3.2}$$

$$\mu/\rho = x^{-1}\ln(I_0/I), \tag{3.3}$$

where I, I_0, μ, and x are transmitted photon intensity, incident photon intensity, density and mass thickness. Generally we call μ/ρ X-ray mass attenuation coefficient. The calculated transmissivity using X-ray mass attenuation

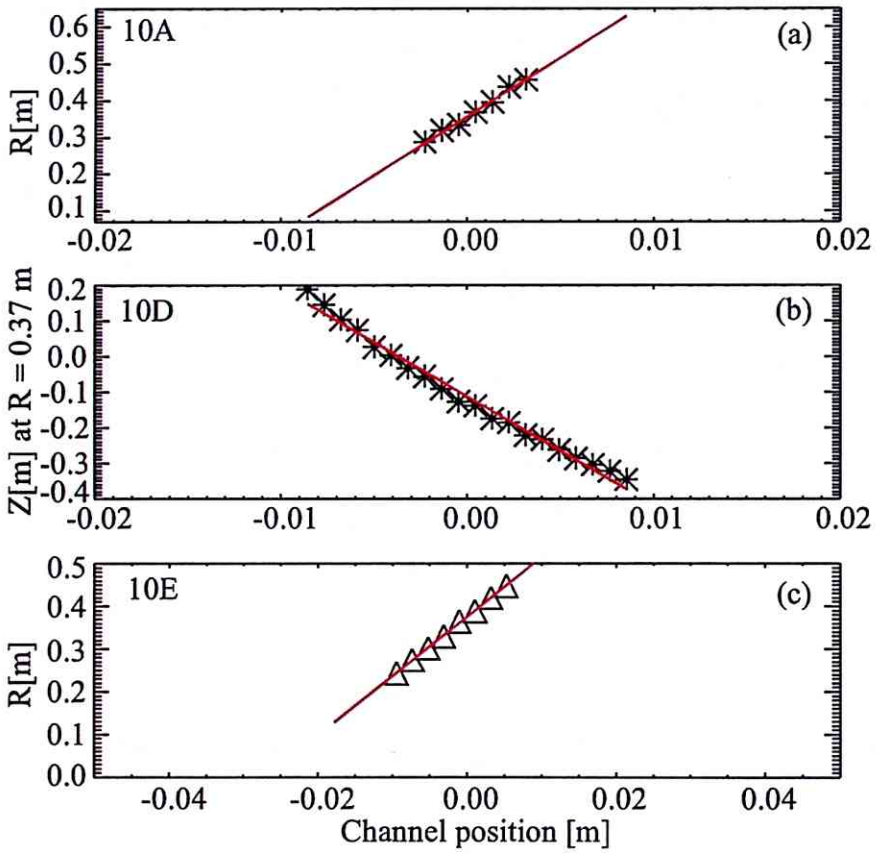

Figure 3.18: Results of alignment for SXR cameras at PORT10-A(a) D(b) and E(c). Each horizontal axis indicates coordinates of each channel.

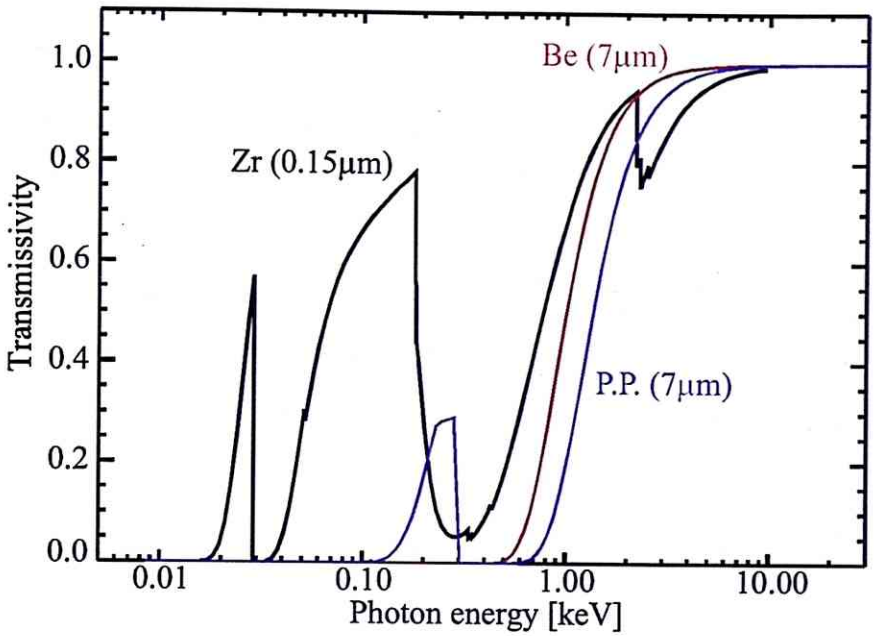

Figure 3.19: Transmissivity of zirconium (0.15 μm), beryllium(7 μm) and polypropylene(7 μm).

coefficient from [75] shown in Fig.3.19. As is indicated above, beryllium cut less than 1 keV photons and applicable for high temperature plasma such as $T_e \sim 1\,\mathrm{keV}$. For the TST-2 plasma, zirconium and polypropylene look useful because there are some transmissivity at $\sim 100\,\mathrm{eV}$. Comparing the two filters, zirconium is superior to measure photons with $\sim 100\,\mathrm{eV}$ in terms of good transmissivity at $\sim 100\,\mathrm{eV}$. Moreover, to induce one electron-hole pairs in semi-conductor, it needs 3.65 eV energy from incident photons. Therefore even we do not use the filters, it is not impossible to measure mode behavior near by the core of the plasma under the such low temperature condition.

3.3 Hard X-ray measurements

3.3.1 Purpose and principle of operation

NaI(Tl) scintillators are sensitive to hard X-rays (> 20 keV) and γ-rays (> 100 keV), and are used to measure high-energy photons[76][77]. These hard X-rays and γ-rays are produced by collision of high-energy electrons with solid material such as the vaccume vessel wall or by bremsstrahlung from energetic electrons in the plasma. It can also be used to study the dynamics of plasma disruption and reconnection events, since energetic electrons are lost during such events.
Scintillators convert X-ray energy into visible light which is proportional to the photon energy. A NaI(Tl) crystal is used in this experiment. Tl(thallium) is necessary for the visible light emission. The NaI(Tl) crystals are weak against heat shock and temperature gradient, and is hygroscopic so it needs to be enclosed. The visible light is converted to electronic signal by use of a photomultiplier tube (PMT). A schematic of PMT is shown in Fig. 3.20. Photons from the scintillator strike the photocathode material, and electrons are produced by the photoelectric effect. These electrons are directed to dynodes and accelerated by the electric field. Secondary electrons are generated and the number of electrons multiplies successively. The multiplied electrons finally strike the anode and electric current is produced.

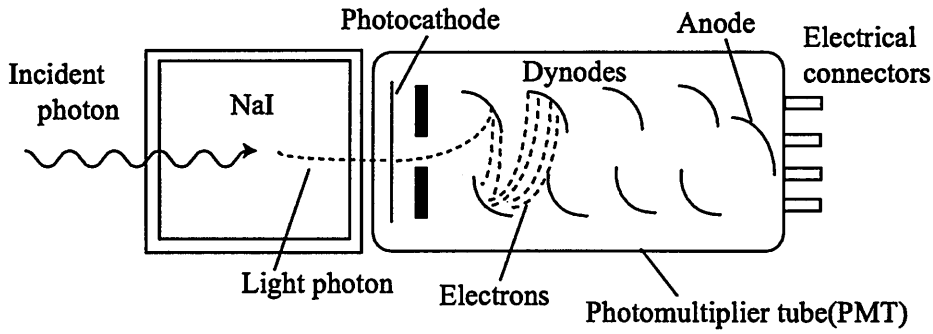

Figure 3.20: Schematic of photomultiplier tube.

The relationship between the ADC output (output signal) and the detected photon energy must be determined for the NaI scintillator system. Calibration was performed using known radiation sources, ^{137}Cs (662 keV) and ^{57}Co (122 keV and 136 keV) [51]. The results of the calibration from [51] with using these sources is shown in Fig.3.21. The fitted line is given by linear fitting using the points at (0 V, 0 keV), (0.04 V, 129 keV (^{57}Co)), and (0.21 V,

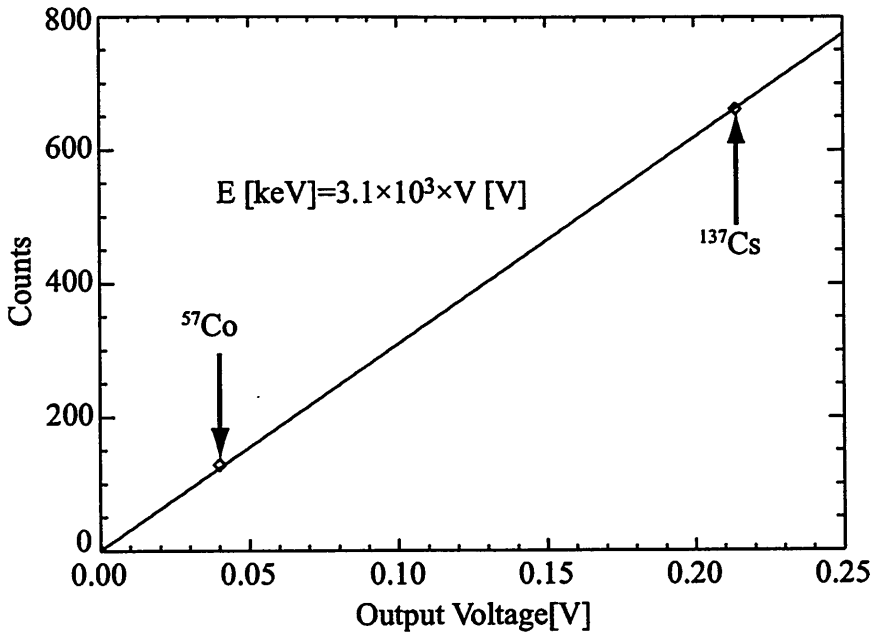

Figure 3.21: Calibration results for NaI(Tl) scintillator. Fitted line is given by (0 V, 0 keV), (0.04 V, 129 keV (^{57}Co)), and (0.21 V, 662 keV (^{137}Cs)).

662 keV (^{137}Cs)). From the fitting results, we can determine the relationship between energy of incident photon (E) and output voltage (V).

3.4 Magnetic measurements

Almost all plasma experiments use magnetic measurements because it is very fundamental, important and easy to install experiments. And, it is one of the most important role of this thesis. Especially magnetic fluctuation measurements can be effective for understanding external magnetic fields. Of course, for equilibrium reconstruction, measurements magnetic fields is essential. In this section introduction of magnetic coil (Mirnov coil) and its applications for acquiring a lot of parameters in plasmas.

Principle of the measurements for magnetic probes

Local magnetic fields can be measured using small coils. Figure 3.22 illustrates easy picture of an example of a magnetic coil. If there are some change

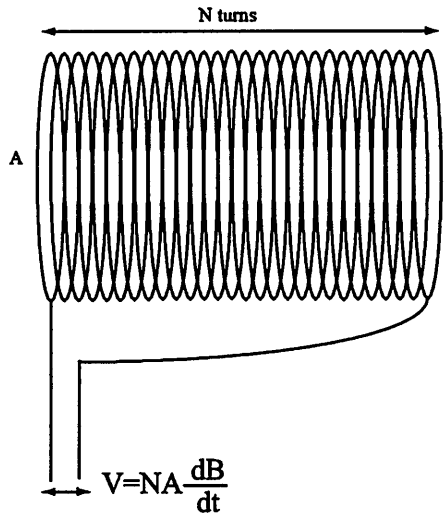

Figure 3.22: Image of magnetic coil.

of magnetic fields with respect to the time, from Maxwell eq. (Faraday's law), following voltage V is induced.

$$V = -NA\frac{\partial B}{\partial t}, \tag{3.4}$$

where N, A and B are the number of turns of the magnetic coil, the area of the magnetic loop and magnetic field, respectively. By integrating the voltage, we can acquire magnetic flux(Φ).

$$\Phi = -\int_{t_0}^{t} V(\acute{t})d\acute{t} \tag{3.5}$$

Magnetic fields **B** are calculated by the Φ.

$$\mathbf{B} \cdot \mathbf{n} = \frac{\Phi}{NA} \tag{3.6}$$

Mirnov coils array: n coils

n coils on TST-2 are an array of magnetic probes (Mirnov coils) for identification of toroidal mode number (n). The configuration of the n-coils are shown in Fig. 3.11. The number of the coils is 8 at the most. Toroidal position of each channels are $\phi = 0°, 30°, 90°, 112.5°, 127.5°, 157.5°, 180°, 220°$. All coils are at $Z = -0.44\,\mathrm{m}$ and $R = 0.592\,\mathrm{m}$.

Mirnov coils array: m coils

m coils are for understanding of poloidal mode structure with 9 channel at the most. However, it is not easy to identify the poloidal mode number (m). The radius and height are 10 mm and 20 mm, respectively. The shape of each coil is cylindrical column. The coils are wired on long-teflon stick in order to prevent errors in setting angles and positions. Figure 3.23 shows the configuration of magnetic probes. The magnetic probes with 37 channels are fixed at a poloidal cross section in the vacuum vessel. For inboard side, there are CP1-CP12, for outboard side, OP1-OP11. For upper side, UP1-UP8, for bottom side BP1-BP8. As other magnetic measurements, flux loops measure the poloidal flux directly. The loops is circular shaped and set along poloidal direction. (the directions of loops are toroidal direction.) Along the centre stack, C1 - C13 are wired, U1 - U10 are on top side, B1 - B10 are on bottom side, O1 and O2 are outboard side. The trunking of the wires made of teflon in order to prevent affects to vacuum environment. In addition to that the wires are protected by the stainless pipes (SUS304). The poloidal flux $\Psi(R, Z)$ is defined as flux passing the area S along a position of (R,Z) on cylindrical coordinate system.

$$\Psi(R, Z) = \int \mathbf{B} \cdot \mathrm{dS} = 2\pi \int_0^R r B_z(R, Z) dr \tag{3.7}$$

3.5 Measurements of ion temperature using spectroscopy

3.5.1 Doppler broadening

Doppler broadening is often used for determination of ion temperature and flow (velocity) of impurities in the plasma. The impurities in the plasma

emit line radiation. When we assume a thermal equilibrium, we can express the velocity distribution along any direction is described by the following Gaussian[31].

$$P(v; v_0, T_i) = A \exp\left(\frac{-m(v-v_0)^2}{2kT_i}\right), \tag{3.8}$$

where A, v, v_0, T_i and m are a factor for normalization of the line emission, velocity (variable), the average velocity, the ion temperature and the mass, respectively. This formula indicates the Doppler broadening. The shape (peaked or flattened) of this function depend on the ion temperature. At high temperature, we obtain flattened distribution. When the impurities move by the plasma flow with a velocity v from the observer, the observed frequency is not simple due to Doppler shift and expressed by this equation.

$$\nu' = \left(1 \pm \frac{v}{c}\right)\nu_0, \tag{3.9}$$

where, ν', c and ν_0 are observed frequency, velocity of light, initial velocity (observed frequency if the observer moves with same velocity v), respectively. Since

$$(v-v_0)^2 = (\nu'-\nu_0)^2\frac{c^2}{\nu_0^2}, \tag{3.10}$$

we obtain the following formula with frequency of the line (ν) by substituting Eq. 3.10 into Eq. 3.8.

$$P(\nu; \nu_0, T_i) = A \exp\left(\frac{mc^2}{2kT_i}\left(\frac{\nu-\nu'}{\nu_0}\right)^2\right), \tag{3.11}$$

indicating ion temperature is obtained by the full width half maximum (W_{FWHM}) on the spectrum.

$$W_{FWHM} = \sqrt{2\ln 2 \cdot \frac{kT_i}{m}}. \tag{3.12}$$

3.5.2 Setup of spectroscopy system

TST-2 is equipped with a spectroscopy system for measurements of ion temperature. The system consist of three parts, mainly.

1. Optical system which collects the light from the plasma, transmit and collect for the slit before the spectroscope.

Two collective lens focus on the centre of the plasma and collect photons and two mirrors steer the light to the slit.

2. Spectrometer which uses diffraction grating for spectrum of incident photons from ultraviolet to visible light.
The image in the spectrometer is shown in Fig. 3.24. Photons through the slit 1 are changed to parallel light at the spherical mirror 1 and reflected at the flat mirror 2. After that, the lights incident to the diffraction grating and are dispersed. The rate of lines and sensitive area of the diffraction grating are 1800 l/mm and $102 \times 102\,\mathrm{mm}^2$, respectively. The dispersed lights are collected at the spherical mirror 3 and pass the slit 2 to detectors (PMT).
3. Detector which measure the intensity of the incident photons through the spectrometer.
The detector is multi-anode type PMT (photo multiplier tube) with 11 channels and its 11 channels measure the photons with every 0.17nm. The sampling rate for output signals from PMT is 1 MHz at the most. Therefore it is possible to measure fast behavior of ion temperature. In this thesis, impurity emission from oxigen (OV) is employed to measure the time evolution of these ion temperature. The "OV" is line spectrum at 278.1 nm emitted from positive ion O^{4+}.

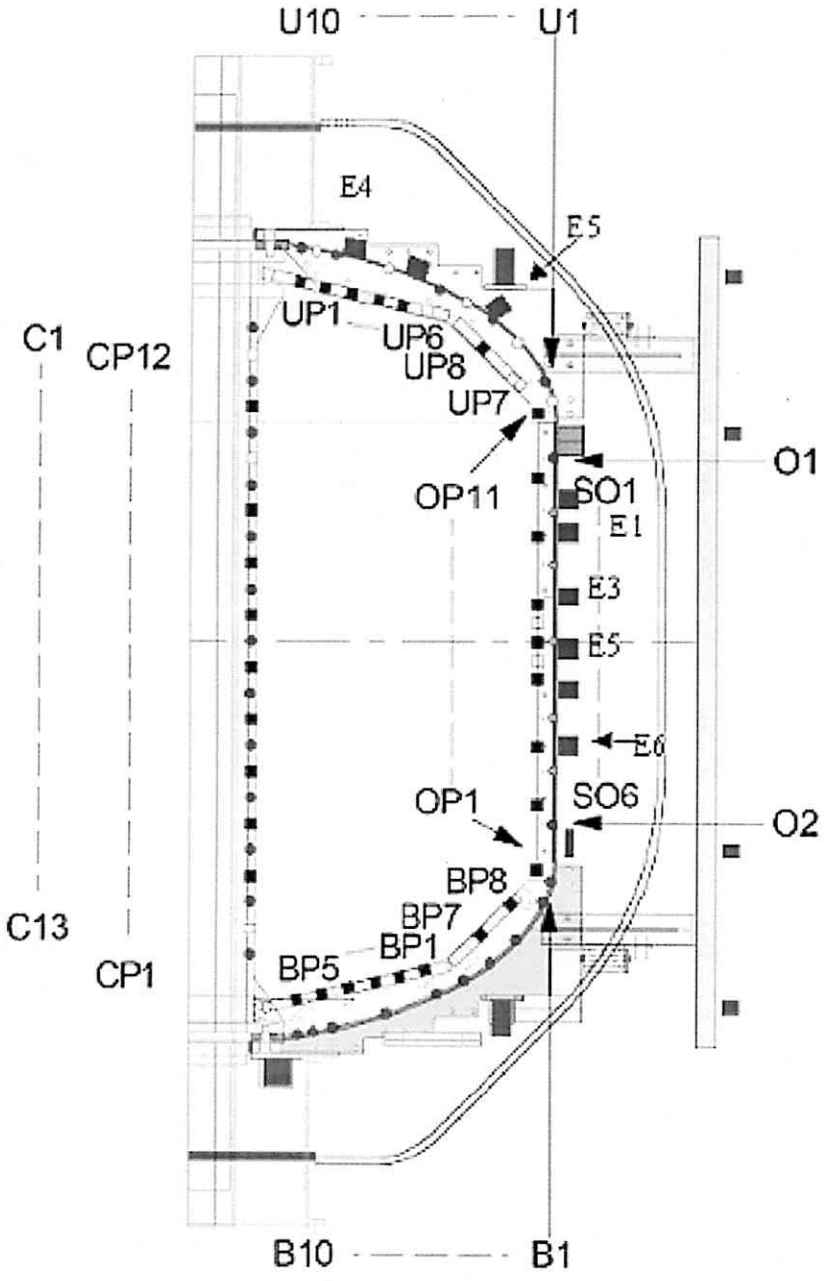

Figure 3.23: Configuration of magnetic probes in TST-2

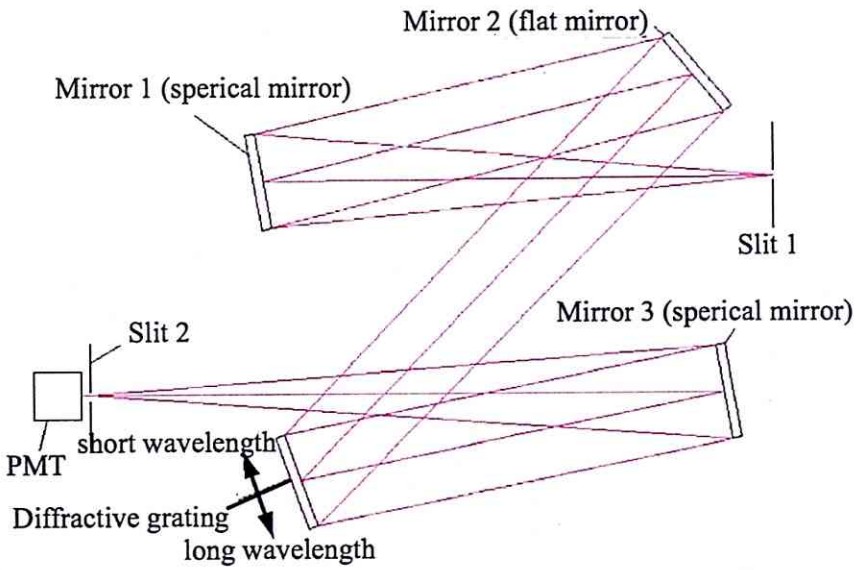

Figure 3.24: Configuration in the spectrometer.

3.6 Tools for mode analysis

3.6.1 Singular value decomposition

Singular value decomposition (SVD) is a useful method in order to extract coherent modes and to understand behavior of fluctuations, such as magnetic fluctuation and density perturbation induced by precursors from MHD instabilities[78][80]. SVD does not require any assumptions about the spatial information of target modes, but can determines its own basis vectors indicating the fluctuation data in the directions of maximum coherence. With coherent signals at various locations we can obtain both the coherent spatial structure and the time evolution of target modes. From mathematical point of view, SVD essentially solves for eigenvectors and eigenvalues of the covariance matrix of a data matrix.

First, consider a matrix $A(M \times N)$, which can be expressed as

$$A = U\Sigma V^T \tag{3.13}$$

where $U(M \times M)$ and $V(N \times N)$ are orthogonal matrices and $\Sigma(M \times N)$ is a diagonal matrix. By using column vectors $\vec{u}_i$ and $\vec{v}_i$, this can be expressed as

$$A = \begin{bmatrix} \vec{u}_1 & \vec{u}_2 & \dots & \vec{u}_M \end{bmatrix} \begin{bmatrix} \sigma_1 & & & & \\ & \sigma_2 & & 0 & \\ & & \ddots & & 0 \\ & 0 & & \ddots & \\ & & 0 & & \sigma_M \quad 0 \end{bmatrix} \begin{bmatrix} \vec{v}_1 \\ \vec{v}_2 \\ \vdots \\ \vdots \\ \vec{v}_N \end{bmatrix} \tag{3.14}$$

This equation indicates that A can be expressed as the sum of $\sigma_i u_i {v_i}^T$ as following equation.

$$A = \sum_{i=1}^{p} \sigma_i \mathbf{u_i v_i^T}, \tag{3.15}$$

where $p = \max(M, N)$ and σ_i is called "sigular value". $A_i = \sigma_i \mathbf{u_i v_i}$ is a matrix $(M \times N)$ same as A and A_i has orthonormality in terms of two dimensional image. In this sense, the matrix A is sum of the image A_i as base, and the singular values σ_i are expansion factors. The $u_i {v_i}^T$ shows fundamental image. In other words, $\mathbf{u_i v_i^T}$ is similar to unit vector and A is expressed by different unit vectors by the linear factor σ_i. If σ_i shows high value, image expressed by $\mathbf{u_i v_i^T}$ is dominant. An image for easy understanding is shown in Fig. 3.25 from [78]. Equation 3.15 satisfy Parseval relation. When we as-

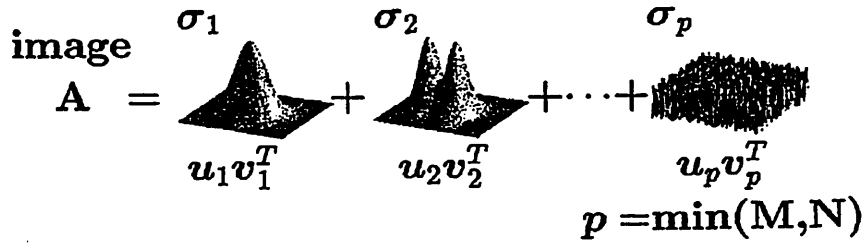

Figure 3.25: Series expansion of a 2-dimensional image A with bases A_i.

sume all energy of A as sum-squared elements a_{ij}, it equals to sum-squared of the factors σ_i.

$$\sum_{i=1}^{M}\sum_{i=1}^{N} = \sum_{i=1}^{p} {\sigma_i}^2 \tag{3.16}$$

When we use N detectors (the number is N) with M time points for measurements plasma fluctuations. The signal matrix can be made as

$$S = \begin{bmatrix} s_1(0) & s_2(0) & \dots & s_N(0) \\ s_1(\Delta t) & s_2(\Delta t) & \dots & s_N(\Delta t) \\ \vdots & \vdots & & \\ \vdots & \vdots & & \\ s_1((M-1)\Delta t) & s_2((M-1)\Delta t) & \dots & s_N((M-1)\Delta t) \end{bmatrix} \tag{3.17}$$

where $\vec{s}_n(m\delta t)$ is a signal from nth detector at mth time point. $(1 \leq n \leq N, 0 \leq m \leq M-1)$ Generally in measurements $M \gg N$ due to limits of the number of detectors. By use of $A = U\Sigma V^T$ in Eq. 3.13, the singular value and decomposed matrices $\mathbf{u_i}$ and $\mathbf{v_i}^{\mathbf{T}}$. $\mathbf{u_i}$ and $\mathbf{v_i}$ are called as *chrono* and *topo* because they indicate base of time evolution and spatial distribution, respectively.

The main advantage of the SVD analysis compared with Fourier analysis is the ability to identify coherent modes in terms of minimum basis vectors and examine the dynamics of these vectors. These vectors may have a complicated spatial structure. SVD is very effective also for removing noise. The singular values σ_i mean power for each decomposed mode. Therefore when we remove such mode with low σ_i and reconstruct the clear signal matrix.

$$\acute{S} = \sum_{i=1}^{q} \sigma_i \mathbf{u_i} {\mathbf{v_i}}^{\mathbf{T}}, \tag{3.18}$$

q is smaller number than N. Owing to such merits plenty of experiments and analysis use SVD. First, in Ref. [78] they confirmed that removing noise

is possible on the signals from electron temperature fluctuation measured by electron cyclotron emission[79] at sawteeth oscillation instability in JT-60U. Reference [80] shows first application of SVD to MHD instabilities and rotating m/n =4/1 and 5/2 modes from magnetic fluctuations. In also DIII -D, SVD has been executed for signals from the Mirnov cois. An application to SXR profiles is also given in the WT-3 tokamak[81]. They employed SXR computer tomography system with plenty of channels of SXR detectors[82] and showed internal mode behavior during MHD instabilities. In most SVD analyses on other fusion devices, only SXR or magnetic signals are used. In our case, however, not only magnetic signals from pick-up coils distributed along the toroidal and poloidal directions but also SXR signals are sometimes used in order to compare and examine external and internal mode structure. This analysis will be shown in next chapter.